

# IMAGING AND SPECTROSCOPIC OBSERVATIONS OF A TRANSIENT CORONAL LOOP: EVIDENCE FOR THE NON-MAXWELLIAN $\kappa$ -DISTRIBUTIONS

JAROSLAV DUDÍK<sup>1</sup>

Astronomical Institute of the Academy of Sciences of the Czech Republic, Fričova 298, 251 65 Ondřejov, Czech Republic

ŠIMON MACKOVJAK<sup>2,3</sup>

ISDC - Data Centre for Astrophysics, Astronomy Department, University of Geneva, Chemin d'Ecogia 16, 1290 Versoix, Switzerland

ELENA DZIFČÁKOVÁ

Astronomical Institute of the Academy of Sciences of the Czech Republic, Fričova 298, 251 65 Ondřejov, Czech Republic

GIULIO DEL ZANNA

DAMTP, CMS, University of Cambridge, Wilberforce Road, Cambridge CB3 0WA, United Kingdom

DAVID R. WILLIAMS

University College London, Mullard Space Science Laboratory, Holmbury St Mary, Dorking, Surrey RH5 6NT, United Kingdom

MARIAN KARLICKÝ

Astronomical Institute of the Academy of Sciences of the Czech Republic, Fričova 298, 251 65 Ondřejov, Czech Republic

HELEN E. MASON

DAMTP, CMS, University of Cambridge, Wilberforce Road, Cambridge CB3 0WA, United Kingdom

JURAJ LÖRINČÍK

DAPEM, Faculty of Mathematics Physics and Computer Science, Comenius University, Mlynská Dolina F2, 842 48 Bratislava, Slovakia

PAVEL KOTRČ, FRANTIŠEK FÁRNÍK, AND ALENA ZEMANOVÁ

Astronomical Institute of the Academy of Sciences of the Czech Republic, Fričova 298, 251 65 Ondřejov, Czech Republic

*Draft version February 28, 2022*

## ABSTRACT

We report on the *SDO/AIA* and *Hinode/EIS* observations of a transient coronal loop. The loop brightens up in the same location after the disappearance of an arcade formed during a B8.9-class microflare three hours earlier. *EIS* captures this loop during its brightening phase as observed in most of the *AIA* filters. We use the *AIA* data to study the evolution of the loop, as well as to perform the DEM diagnostics as a function of  $\kappa$ . Fe XI–Fe XIII lines observed by *EIS* are used to perform the diagnostics of electron density and subsequently the diagnostics of  $\kappa$ . Using ratios involving the Fe XI 257.772Å selfblend, we diagnose  $\kappa \lesssim 2$ , i.e., an extremely non-Maxwellian distribution. Using the predicted Fe line intensities derived from the DEMs as a function of  $\kappa$ , we show that, with decreasing  $\kappa$ , all combinations of ratios of line intensities converge to the observed values, confirming the diagnosed  $\kappa \lesssim 2$ . These results represent the first positive diagnostics of  $\kappa$ -distributions in the solar corona despite the limitations imposed by calibration uncertainties.

*Keywords:* Techniques: spectroscopy – Radiation mechanisms: non-thermal – Sun: corona – Sun: UV radiation – Sun: X-rays, gamma rays

## 1. INTRODUCTION

jaroslav.dudik@asu.cas.cz

<sup>1</sup> RS Newton International Fellow, DAMTP, CMS, University of Cambridge, Wilberforce Road, Cambridge CB3 0WA, United Kingdom

<sup>2</sup> DAPEM, Faculty of Mathematics Physics and Computer Science, Comenius University, Mlynská Dolina F2, 842 48 Bratislava, Slovakia

<sup>3</sup> Astronomical Institute of the Academy of Sciences of the Czech Republic, Fričova 298, 251 65 Ondřejov, Czech Republic

The distance and nature of the stellar coronae with temperatures of up to several million Kelvin together with the proximity of the stars themselves make direct probing of these environments impossible at present. In the absence of in-situ measurements, the emitted spectrum remains the only source of information about the physical conditions in these emitting media. Most of the coronal radiation is emitted in the X-ray, extreme ultraviolet (EUV) and ultraviolet parts of the electro-

magnetic spectrum, requiring space-borne observatories. This poses further problems with limited availability of the data, calibration and its stability (BenMoussa et al. 2013; Del Zanna 2013a), as well as the unavoidable trade-offs between the spatial, temporal, and spectral resolutions and coverages.

In many instances, it is advantageous to combine imaging and spectroscopic observations (e.g., Schmelz et al. 2009; Warren et al. 2012; Del Zanna 2013b). Imaging observations employing narrow-band EUV filters, such as those made by the Atmospheric Imaging Assembly (AIA, Lemen et al. 2012; Boerner et al. 2012) onboard the *Solar Dynamics Observatory* (*SDO*, Pesnell et al. 2012), offer high spatial and temporal resolution. These are complemented with spectroscopic observations made in similar wavelength ranges, such as those performed by the EUV Imaging Spectrograph (EIS, Culhane et al. 2007) onboard the *Hinode* spacecraft (Kosugi et al. 2007). Traditionally, the vast majority of both the imaging and spectroscopic data are analyzed and modelled under the assumption of the local equilibrium, i.e., Maxwellian distribution of particle energies. This is because calculation of the synthetic spectra requires integration of many individual ionization, recombination, excitation and deexcitation cross-sections over the (unknown) distribution function in order to obtain rates of these processes and finally the corresponding emissivities at individual wavelengths. The assumption of Maxwellian distribution affords easy calculation of the synthetic spectra, e.g., using the CHIANTI atomic database and software (Dere et al. 1997; Landi et al. 2013).

However, this assumption is incorrect if there are correlations between the particles in the system. Such correlations can be induced by any long-range interactions in the system (Collier 2004; Leubner 2004; Livadiotis & McComas 2009, 2010, 2013), e.g., particle acceleration due to magnetic reconnection (e.g., Zharkova et al. 2011; Petkaki & MacKinnon 2011; Stanier et al. 2012; Cargill et al. 2012; Burge et al. 2012, 2014; Gordovskyy et al. 2013, 2014), shocks, or wave-particle interactions (e.g., Vocks et al. 2008). In such cases, the particle distribution will depart from the Maxwellian one, and will likely exhibit an enhanced high-energy tail. Furthermore, turbulence with the diffusion coefficient inversely proportional to particle velocity will also lead to the appearance of the non-Maxwellian distributions with characteristic high-energy tails (e.g., Hasegawa et al. 1985; Laming & Lepri 2007; Bian et al. 2014). We note that the collision cross-section scales with  $E^{-2}$ , where  $E$  is the particle energy (Meyer-Vernet 2007). This leads to the behaviour of the collision frequency as  $E^{-3/2}$ , i.e., the high-energy tail is difficult to equilibrate. Therefore, the currently favoured theories of nanoflare heating of the solar corona (Klimchuk 2006; Klimchuk et al. 2010; Tripathi et al. 2010; Bradshaw et al. 2012; Winebarger 2012; Viall & Klimchuk 2011a,b, 2013) should afford situations for departures from the Maxwellian distribution. Scudder & Karimabadi (2013) argue that the particle distribution in the solar and stellar coronae above  $1.05R_{\odot}$  is strongly non-Maxwellian.

Observational clues that the solar corona could be non-Maxwellian come from the in-situ detection

of the non-Maxwellian  $\kappa$ -distributions in the solar wind (Collier et al. 1996; Maksimovic et al. 1997a,b; Zouganelis 2008; Le Chat et al. 2011). Spectroscopic evidence for the presence of  $\kappa$ -distributions in the transition region was found from active region Si III spectra (Dzifčáková & Kulinová 2011). The  $\kappa$ -distributions are characterized by a high-energy power-law tail (Sect. 2), with the power-law index being given by the value of  $-(\kappa + 1/2)$ . In the solar wind, the typically detected values are  $\kappa \gtrsim 2.5$ , while the detection in the transition region yielded  $\kappa \approx 7$  from the active region Si III spectrum. Presence of high-energy electrons in the transition region at the base of coronal loops have recently been established also by Testa et al. (2014) by analyzing the transition-region Si IV emission observed by the IRIS instrument (De Pontieu et al. 2014).

Despite these detections in the solar wind and the transition region, no direct, unambiguous detection of the non-Maxwellian distribution in the coronal spectra have been made to date. Attempts at doing so were made e.g. by Feldman et al. (2007), Ralchenko et al. (2007), Hannah et al. (2010), Dzifčáková & Kulinová (2010), and Mackovjak et al. (2013). Feldman et al. (2007) assumed a bi-Maxwellian distribution, with the temperature of the second Maxwellian chosen to be 10 MK, and argued that no such second Maxwellian is necessary to explain the observed spectra of He-like lines. This analysis was however limited and did not include the effects of  $\kappa$ -distributions on the spectra. Ralchenko et al. (2007) showed that the quiet-Sun Si, Ca, and Ar spectra are consistent with a bi-Maxwellian distribution, where the second Maxwellian contains only a small fraction of particles, of the order of several per cent. Its temperatures range from 2.3 MK (300 eV) to 7.7 MK (1000 eV), with the fraction of particles being at most 5–7%, and 1% for these temperatures, respectively. No diagnostics of  $\kappa$  was performed. Hannah et al. (2010) used off-limb quiet-Sun observations performed by the RHESSI spacecraft (Lin et al. 2002) to constrain the emission measures corresponding to individual power-law and  $\kappa$ -distributions. However, the constraints obtained on the emission measures were rather large even for small values of  $\kappa$ . Dzifčáková & Kulinová (2010) and Mackovjak et al. (2013) studied the possibilities of diagnosing  $\kappa$  using lines observed by EIS. Despite having found several combinations of line ratios sensitive to  $\kappa$ , mostly involving neighbouring ionization stages, unambiguous detection were difficult due to atomic data uncertainties and possible multi-thermal effects along the line-of-sight that were not accounted for. Subsequently, Mackovjak et al. (2014) showed that the techniques to obtain the differential emission measures work also for the  $\kappa$ -distributions, and studied the influence of  $\kappa$  on such analyses.

In this paper, we use the imaging and spectroscopic observations performed by *SDO/AIA* and *Hinode/EIS* in conjunction with the latest instrument calibration, atomic datasets, and differential emission measure techniques to analyze a transient loop observed within an active region core. Spectral synthesis for the non-Maxwellian  $\kappa$ -distribution is briefly discussed in Sect. 2. Analysis of the AIA imaging observations is performed in Sect. 3. In Sect. 4, ratios of spectral lines observed by EIS are analyzed to obtain the electron density and

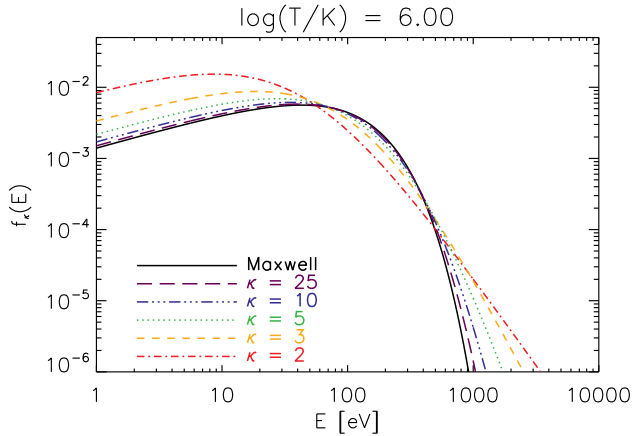


**Figure 1.** The  $\kappa$ -distributions with  $\kappa=2, 3, 5, 10, 25$  and the Maxwellian distribution plotted for  $\log(T/K)=6.0$ . Colors and linestyles denote the different values of  $\kappa$ . A color version of this image is available in the online journal.

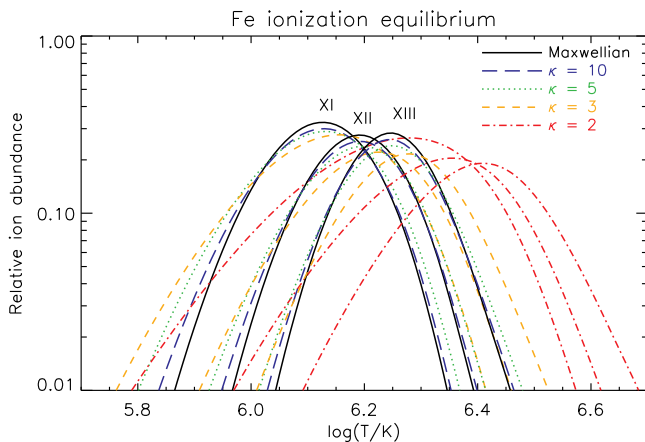


**Figure 2.** Ionization equilibrium for Fe XI–Fe XIII for the  $\kappa$ -distributions, according to the calculations of Dzifčáková & Dudík (2013). A color version of this image is available in the online journal.

$\kappa$  in the loop. Influence of the atomic data uncertainties on the diagnostics are discussed in Sect. 5. The results are summarized and discussed in Sect. 6.

## 2. SYNTHETIC SPECTRA FOR THE $\kappa$ -DISTRIBUTIONS

### 2.1. The Non-Maxwellian $\kappa$ -distributions

The  $\kappa$ -distribution of electron energies (Fig. 1) is defined as a two-parametric distribution with parameters  $T \in (0, +\infty)$  and  $\kappa \in (3/2, +\infty)$  (e.g., Owocki & Scudder 1983; Livadiotis & McComas 2009)

$$f_{\kappa}(E)dE = A_{\kappa} \frac{2}{\sqrt{\pi}(k_{\text{B}}T)^{3/2}} \frac{E^{1/2}dE}{\left(1 + \frac{E}{(\kappa-3/2)k_{\text{B}}T}\right)^{\kappa+1}}, \quad (1)$$

where the  $A_{\kappa} = \Gamma(\kappa+1)/(\Gamma(\kappa-1/2)(\kappa-3/2)^{3/2})$  is the normalization constant and  $k_{\text{B}} = 1.38 \times 10^{-16}$  erg s $^{-1}$  is the Boltzmann constant. The Maxwellian distribution at a given  $T$  is recovered for  $\kappa \rightarrow \infty$ . Maximum departure from the Maxwellian occurs for  $\kappa \rightarrow 3/2$ .

The mean energy  $\langle E \rangle = 3k_{\text{B}}T/2$  of a  $\kappa$ -distribution does not depend on  $\kappa$ . Because

of this,  $T$  can be defined as the temperature. Meyer-Vernet et al. (1995), Livadiotis & McComas (2009) and Livadiotis & McComas (2010) showed that  $T$  indeed has the same physical meaning for the  $\kappa$ -distributions as the (kinetic) temperature for the Maxwellian distribution, and that it also corresponds to the definition of physical temperature in the framework of the generalized Tsallis statistical mechanics (Tsallis 1988, 2009). This permitted these authors to generalize of the zero-th law of thermodynamics for the  $\kappa$ -distributions, and it also permits, e.g., the definition of electron kinetic pressure  $p = n_e k_{\text{B}}T$  in the usual manner.

It is straightforward to see from Eq. (1) that in the high-energy limit, the  $\kappa$ -distribution approaches a power-law with the index of  $-(\kappa+1/2)$ . On the other hand, in the low-energy limit, the  $\kappa$ -distribution behaves as a Maxwellian with  $T_{\text{M}} = T(\kappa-3/2)/(\kappa+1)$ , and scaled to an appropriate constant (see Dzifčáková et al. 2015). Therefore, the  $\kappa$ -distribution can be thought of as a Maxwellian core (at a lower temperature) with a power-law tail.

### 2.2. Line Intensities for the $\kappa$ -Distributions

The emissivity  $\varepsilon_{ji}$  of an optically thin spectral line arising due to a transition  $j \rightarrow i$ ,  $j > i$ , in a  $k$ -times ionized ion of the element  $X$  is given by (e.g., Mason & Monsignori Fossi 1994; Phillips et al. 2008)

$$\varepsilon_{ji} = \frac{hc}{\lambda_{ji}} A_{ji} n(X_j^{+k}) = \frac{hc}{\lambda_{ji}} \frac{A_{ji}}{n_e} \frac{n(X_j^{+k})}{n(X^{+k})} \frac{n(X^{+k})}{n(X)} A_X n_e n_{\text{H}} = A_X G_{X,ji}(T, n_e, \kappa) n_e n_{\text{H}}, \quad (2)$$

where  $h \approx 6.62 \times 10^{-27}$  erg s is the Planck constant,  $c \approx 3 \times 10^{10}$  cm s $^{-1}$  represents the speed of light,  $\lambda_{ji}$  is the wavelength of the resulting spectral line,  $A_{ji}$  the corresponding Einstein coefficient for spontaneous emission,  $n(X_j^{+k})$  is the density of the ion  $+k$  with electron in the excited upper level  $j$ ,  $n(X^{+k})$  the total density of ion  $+k$ ,  $n(X) \equiv n_X$  the total density of element  $X$  whose abundance is  $A_X$ ,  $n_{\text{H}}$  the hydrogen density, and  $n_e$  the electron density. The function  $G_{X,ji}(T, n_e, \kappa)$  is the contribution function for the line  $\lambda_{ji}$ . The  $G_{X,ji}(T, n_e, \kappa)$  is a function of  $\kappa$  due to the dependence of the individual collisional processes of ionization, recombination, excitation and deexcitation on  $\kappa$  (e.g., Dzifčáková 1992; Dzifčáková 2002, 2006a; Wannawichian et al. 2003; Dzifčáková & Mason 2008; Dzifčáková & Dudík 2013; Dudík et al. 2014a,b; Dzifčáková et al. 2015).

The intensity  $I_{ji}$  of the spectral line is then given by the integral of emissivity along a line of sight  $l$

$$I_{ji} = \int A_X G_{X,ji}(T, n_e, \kappa) n_e n_{\text{H}} dl, \quad (3)$$

or

$$I_{ji} = \int A_X G_{X,ji}(T, n_e, \kappa) \text{DEM}_{\kappa}(T) dT, \quad (4)$$

where the quantity  $\text{EM} = \int n_e n_{\text{H}} dl$  is the plasma emission measure, and  $\text{DEM}_{\kappa}(T) = n_e n_{\text{H}} dl/dT$  is the differential emission measure, generalized for the  $\kappa$ -distributions by Mackovjak et al. (2014).

The line intensities for  $\kappa$ -distributions are evaluated using the ionization equilibrium calculations for

$\kappa$ -distributions (Dzifčáková & Dudík 2013). Relative level population is obtained using the approximative method of Dzifčáková (2006b), Dzifčáková & Mason (2008) and Dzifčáková et al. (2015) based on atomic data corresponding to the CHIANTI database, version 7.1 (Dere et al. 1997; Landi et al. 2013). The accuracy of this method for allowed transitions is less than 10% (Dzifčáková & Mason 2008). For the Fe IX–Fe XIII, which are the ions used for diagnostics in Sect. 4, the line intensities are obtained by direct integration of the collision strengths (Dudík et al. 2014b). The collision strengths for these calculations are state-of-the-art and taken from Del Zanna (2010), Del Zanna (2011), Del Zanna et al. (2012b), Del Zanna & Storey (2012), Del Zanna et al. (2012a), Del Zanna & Storey (2013), and Del Zanna et al. (2014).

### 3. SDO/AIA OBSERVATIONS OF A TRANSIENT CORONAL LOOP: IMAGING

The Atmospheric Imaging Assembly (AIA, Lemen et al. 2012; Boerner et al. 2012) on board NASA’s *Solar Dynamics Observatory* (SDO, Pesnell et al. 2012) mission consists of 4 identical, normal-incidence two-channel telescopes with a diameter of 20 cm. AIA provides multiple, near-simultaneous full-Sun images with high temporal (12 s) and spatial resolution (1.5”, pixel size 0.6”). AIA images of the Sun are taken in 10 filters, 7 of which are centered on EUV wavelengths (94Å, 131Å, 171Å, 193Å, 211Å, 304Å, and 335Å), and 3 on UV or visible wavelengths (1600Å, 1700Å, and 4500Å). The EUV filters are centered on some of the strongest Fe lines in the solar EUV spectrum. However, other emission lines originating at different temperatures are present within each filter bandpass. This makes the temperature responses of the AIA EUV filters highly multi-thermal (e.g., O’Dwyer et al. 2010; Del Zanna et al. 2011b; Schmelz et al. 2013).

Compared to the Maxwellian distribution, the AIA responses for  $\kappa$ -distributions are even more multi-thermal (Dzifčáková et al. 2015, Fig. 8 therein). This is mostly caused by the behaviour of the ionization equilibrium (Dzifčáková & Dudík 2013), with the relative ion abundances of individual ions becoming wider and flatter with decreasing  $\kappa$  (see also Fig. 2). Peaks of the individual filter responses can also be shifted towards higher  $T$ , especially for low  $\kappa = 2-3$  (Dzifčáková et al. 2012; Dzifčáková et al. 2015). Typically, in-depth understanding of the AIA observations requires differential emission measure (DEM) analysis, see, e.g., Hannah & Kontar (2012) and Hannah & Kontar (2013).

In the following, we report on the AIA observations of a transient coronal loop and its spatial and temporal relation to the solar microflaring activity. DEM analysis of the AIA data is performed in Sects. 3.3 and its influence on spectroscopic diagnostics is studied in Sect. 4.3.

#### 3.1. Relation of the Transient Loop to Microflaring Activity

The transient loop studied here was observed in the active region (hereafter, AR) NOAA 11704. This active region was a small bipolar AR, of Hale class  $\beta/\alpha$ , characterized by two leading negative sunspots and dispersed plagues of both polarities. On 2013 March 30, a compact

B8.9-class microflare was observed within this AR, peaking at about 10:24 UT (Fig. 3, *top left*). A weaker B4.8 microflare was observed to peak at 13:21 UT in a different AR NOAA 11708. Perhaps by coincidence, during the same time, we observe a transient loop within AR 11704 in the same place as the previous B8.9 microflare (Fig. 3).

Figure 3 and Movie 1 (online) show the location of the B8.9 microflare and the transient loop within the AR 11704 in AIA 171Å channel. The 171Å channel is chosen since it provides the best representation of the morphology of all features. The B8.9 flare was related to a failed eruption of a long intermediate filament. One end of the filament lies within AR 11704, with the filament extending further away in the North-East direction (Fig. 3). The activation of the filament starts at about 10:00 as a series of brightenings within the filament and its immediate neighborhood, subsequently leading to apparently untwisting motions of bright threads. The filament does not erupt however, perhaps due to the overlying field seen e.g. in the AIA 193Å band.

The failed eruption is accompanied appearance of a flare arcade within AR 11704. The arcade first appears in the AIA 131Å band (Fig. 3, *top right*) and subsequently in cooler AIA channels. The arcade is still visible in 171Å an hour later at 11:24 UT and subsequently fades. The fading of the arcade is accompanied by the appearance of falling blobs along the arcade in 304Å (Movie 1) that are visible until about 12:30 UT. After this time, evolving loops are still observed in the same location. The evolution of these loops (Movie 1) resembles slipping reconnection (e.g., Aulanier et al. 2006, 2007, 2012), although this is ambiguous given the presence of many individual loops and other emitting structures. The loop emission at the loci of the flare arcade completely fades out of the AIA 171Å channel at about 12:53 UT. However, at approximately 13:01 UT, a transient coronal loop starts brightening up once more (Sect. 3.2), preceded again by activity in the filament (Fig. 3, *bottom left*). No restructuring of the large-scale magnetic configuration of the AR 11704 is noticeable during the period studied here (09:00–15:00 UT, Fig. 3).

#### 3.2. Multi-wavelength Evolution of the Loop

We now focus on the evolution of the transient loop. The multi-wavelength evolution of the EUV emission is shown in Figure 4 with a cadence of 20 minutes. The emission of the transient loop is observed in AIA 171Å for nearly 2 hours (see also online Movie 1). The images in Fig. 4 are chosen to include the time of 13:19 UT, during which the EIS spectrometer observes a part of the transient loop (Sect. 4).

Upon careful examination, we find spatial misalignments of unknown origin between various AIA bands, especially in Solar  $Y$  direction. These misalignments are corrected for manually by matching the positions of the low-lying moss emission. In this correction, the AIA 171Å and 193Å bands are taken as the reference ones, since no detectable misalignment between these two bands is found. The AIA 211Å is corrected by shifting it by  $\Delta Y = -1.6$  px (1 px  $\equiv 0.6''$ ) to match the 193Å band, which has similar emission morphology. Subsequently, the 335Å band is corrected by shifting it by  $\Delta Y = 2.13$  px

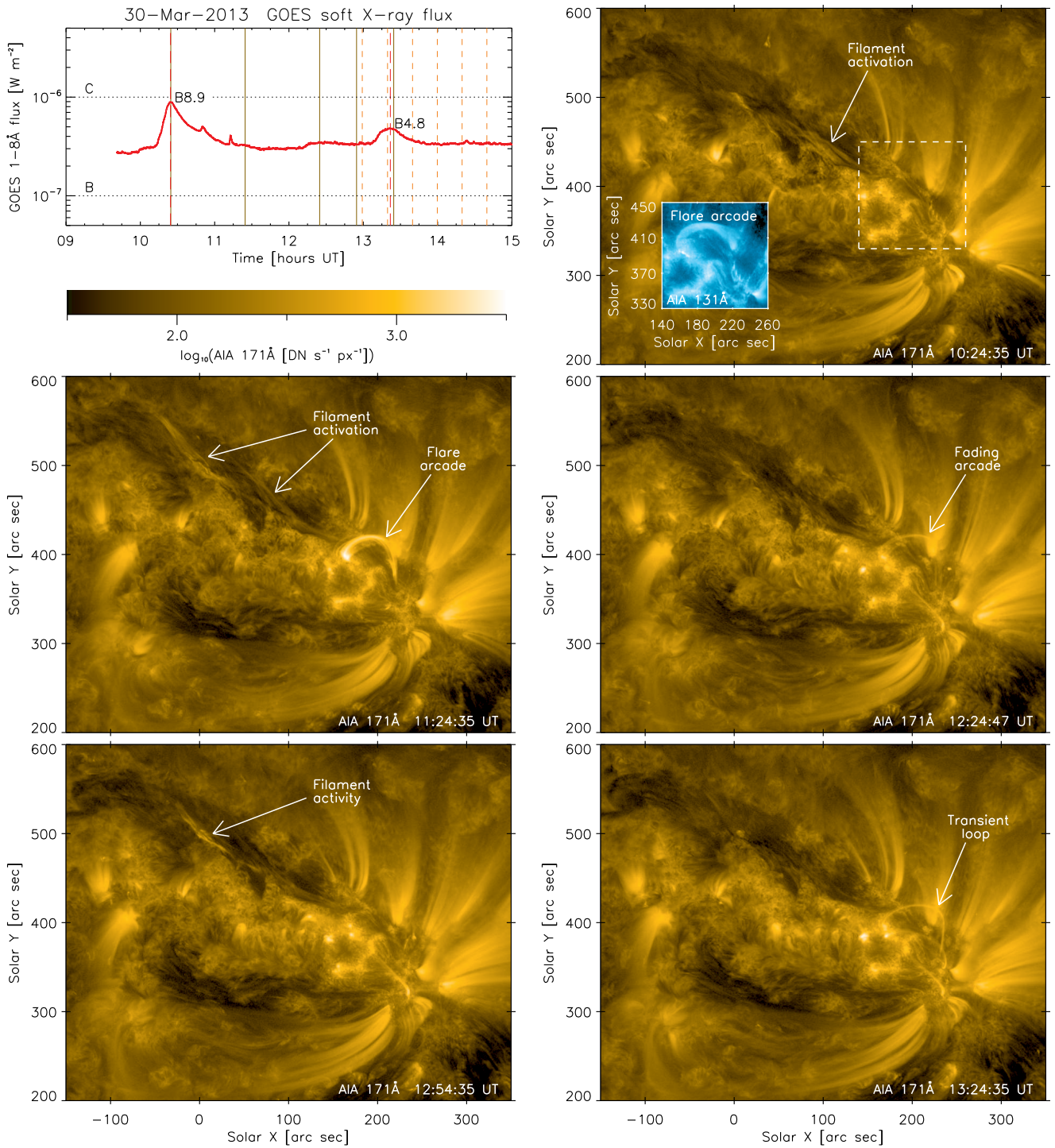


**Figure 3.** Evolution of the two microflares observed by AIA 171Å. *Top left:* GOES X-ray flux at 1–8Å. Red-dashed vertical lines denote the times of the two microflares, full brown lines denote the times of AIA 171Å snapshots, and the orange-dashed lines denote the times of snapshots in Fig. 4. *Inset in top right:* AIA 131Å 1-minute average image showing the arcade of during the B8.9 microflare. The location of the inset corresponds to the box shown.

A color version of this image is available in the online journal.

to match the corrected 211Å band, again due to similar emission morphology. The 131Å band is shifted  $\Delta Y = 1.5$  px to match the 171Å band. No correction is necessary for the 94Å band. After these corrections, the location of the moss emission is the same throughout the AIA bands, and the spatial correspondence of loops observed in different bands is substantially im-

proved as well. We also note that the AIA data shown in Fig. 4 are corrected for solar differential rotation using the *drot\_map* routine available within Solar Soft under IDL.

Before the loop appears in AIA 171Å, it is visible in AIA 335Å, 211Å, and 193Å (Fig. 4, *top row*). The transient loop belongs to the series of evolving loops al-

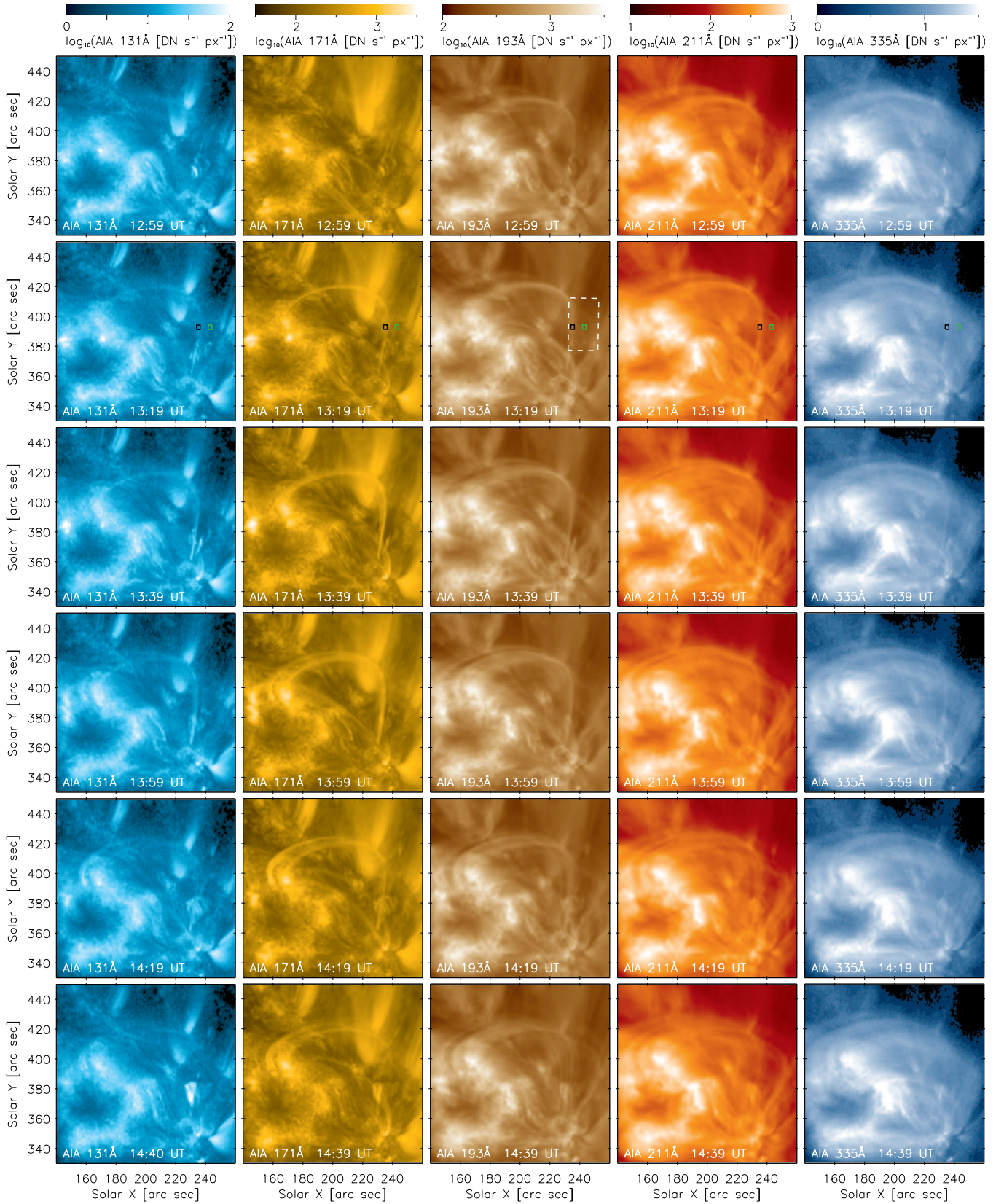


**Figure 4.** Multi-wavelength imaging observations of the loop evolution made by *SDO/AIA*. The time cadence shown is 20 min. AIA data are averaged over 1-minute intervals to increase the signal-to-noise especially in the 335Å and 131Å bands. The images are scaled logarithmically. The field of view shown corresponds to the box in Fig. 3. Small black and green boxes in the *second* row denote the selected portion of the loop and background, respectively. The white box shows the field of view of a portion of the EIS raster shown in Fig. 8.

A color version of this image is available in the online journal.

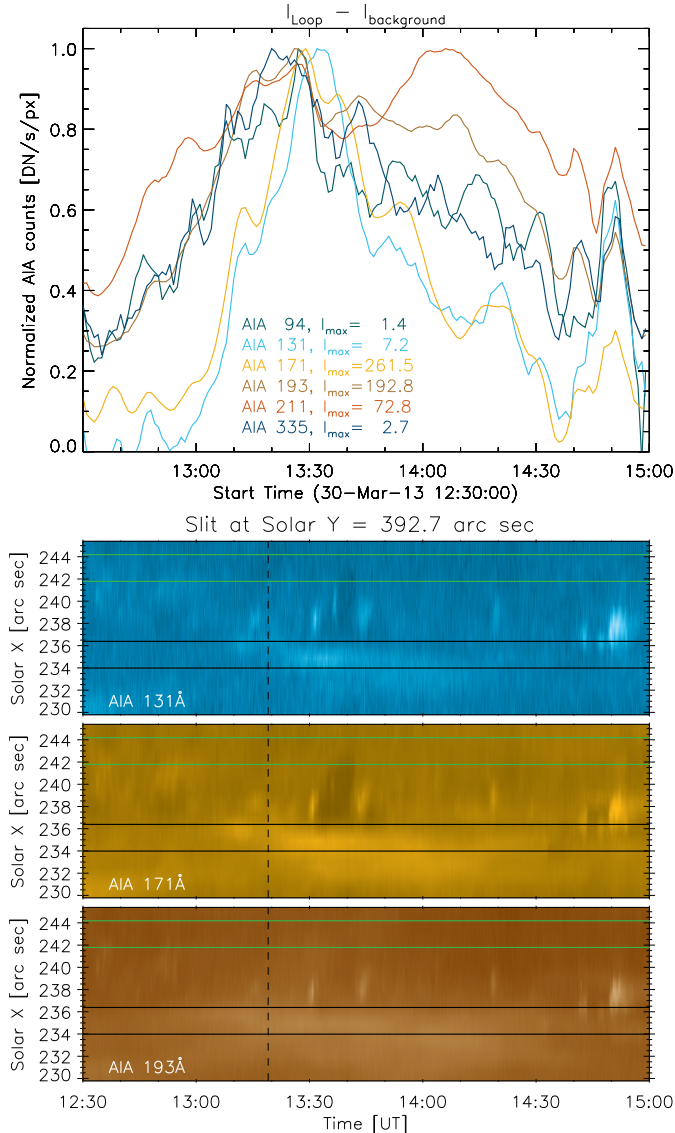


**Figure 5.** *Top:* Background-subtracted intensity lightcurves for the small black box shown in Fig. 4. The lightcurves are normalized to maximum intensity in the time window shown. The maximum intensities are listed for each filter. Individual colors stand for individual AIA filters. *Bottom:* Time-distance plots in AIA 131Å, 171Å, and 193Å along a slit placed through the black and green box at Solar  $Y = 392.7''$ . Black and green horizontal lines correspond to the Solar  $X$  extensions of the respective boxes shown in Fig. 4, where black stands for the loop and green for the background. The vertical dashed black line corresponds to 13:19 UT (Sect. 4). A color version of this image is available in the online journal.

ready present at the same location (Movie 1). At about 13:01 UT (Fig. 5), the loop is discernible as a brightening structure in all AIA EUV channels. In the vicinity of its right footpoint at  $X=235''$ ,  $Y=370''$ , we observe heightened activity (see Movie 1), with the appearance of many bright, short, short-lived closed loops and jetting activity, likely indicating ongoing magnetic reconnection. The transient loop continues to brighten, and at 13:19 UT, corresponding to the time of the EIS observation, the loop is already a prominent emitting structure (Fig. 4, *second row*). The temporal evolution of the loop emission is shown in Fig. 5. The *top* panel of this figure shows background-subtracted lightcurves in a small

black box of  $4 \times 5$  AIA pixels at the position of the loop. The background is represented by the green box of  $4 \times 5$  AIA pixels located to the right of the black box (Fig. 4, *second row*). Its location is chosen so that its intensity is not contaminated by the jet emission (Fig. 5).

The loop emission first peaks in the 335Å filter at about 13:20 UT, followed by 211Å and 193Å at 13:26 UT, and subsequently by 94Å at 13:27 UT, 171Å at 13:29 UT, and 131Å at 13:32 UT that order. I.e., the emission first peaks in Fe XVI and subsequently cools down to Fe VIII observed in 131Å. This is important, since these results show that no hot flare-like emission is present. If it were, it would be detected as Fe XXI and Fe XVIII emission in the AIA 131Å and 94Å bands (e.g., Del Zanna et al. 2011a; Petkaki et al. 2012) prior to the maximum of the 335Å lightcurve. The 94Å emission is observed to be very weak, of the order of several  $\text{DN s}^{-1} \text{px}^{-1}$ , suggesting absence of strong, dense plasma emitting in Fe XVIII. The 131Å emission closely follows the 171Å, showing that it is dominated by Fe VIII. This conclusion is confirmed using the time-distance plots constructed as a function of Solar  $X$  using a slit placed at Solar  $Y = 392.7''$ , i.e., through the centres of the black and green boxes (Fig. 4, *second row*).

We note that the lightcurves show multiple peaks. This is most likely due to the multi-thermal nature of the AIA bands. In principle, DEM analysis can help identify the contributions to individual peaks, if the distribution function (i.e., value of  $\kappa$ ) is known. Since  $\kappa$  cannot be determined from AIA data alone (Sect. 3.3), we do not perform this analysis.

We also note that the loop evolution is accompanied by presence of multiple jets originating near the loop’s right (western) footpoint (Movie 1). With increasing height, these jets diverge from the loop and thus do not contaminate the loop emission. In Fig. 5, *bottom*, the jets appear as a series of fast-moving, short-lived brightenings near the position of the loop (black horizontal lines). The jetting activity starts at about 13:14 UT and extends beyond the lifetime of the transient loop.

With increasing time, the loop evolves into a series of individual threads and subsequently fades away (Figs. 4, 5, and Movie 1).

### 3.3. Multithermality of the Loop as a function of $\kappa$

Since the loop is observed in all six AIA coronal EUV bands, it is expected to be multi-thermal. We used the regularized inversion method of Hannah & Kontar (2012, 2013) to obtain the DEMs as a function of  $\kappa$ . The results are shown in Figs. 6 and 7.

The  $\text{DEM}_\kappa$  reconstruction is performed for each pixel of the 1-minute averaged AIA data observed at 13:19 UT (Fig. 4, *second row*). Before the DEM reconstruction, we remove the stray light from the AIA data using the method of Poduval et al. (2013). In the DEM reconstruction, a temperature interval of  $\log(T/\text{K}) = 5.5 - 7.4$  ( $\Delta \log(T/\text{K}) = 0.1$ ) is used. The value of  $\kappa$  is assumed to be constant throughout the field of view. We note that such assumption may not be justified, as individual emitting and indeed overlapping structures could in principle have different values of  $\kappa$ . However, in the absence of simultaneous stereoscopic *and* spectroscopic observations throughout the field of view, it is not possible to

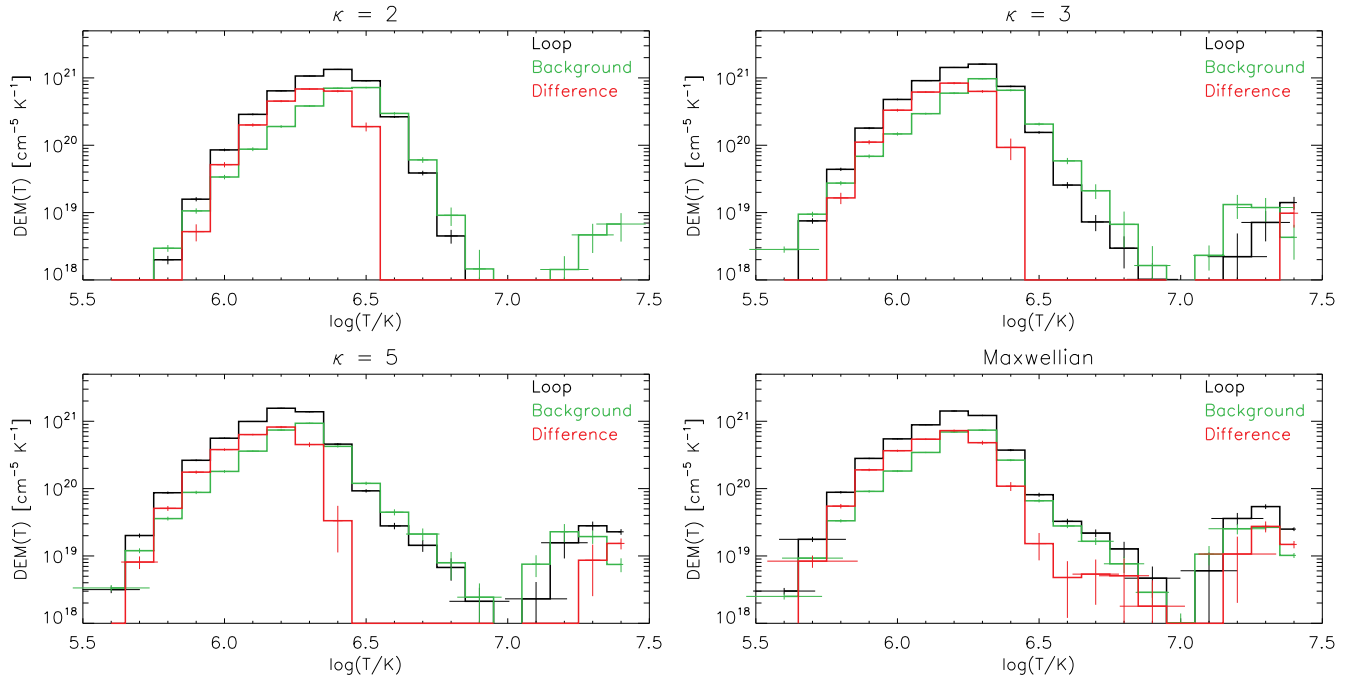


**Figure 6.** DEM diagnostics from AIA data using the regularized inversion method. The distribution assumed is indicated at each panel. Black and green lines stand for the average DEMs within the black and green boxes in Fig. 4. Red stands for their difference. Uncertainties of the DEMs in each temperature bin are given by the respective horizontal and vertical error bars. A color version of this image is available in the online journal.

obtain the value of  $\kappa$  for each emitting structure in each pixel at a given time; an assumption is therefore necessary. By adopting a single value of  $\kappa$  for the entire field of view, we demonstrate the feasibility of the regularized inversion method to recover the non-Maxwellian DEMs from AIA observations using the corresponding responses for the  $\kappa$ -distributions (Dzifčáková et al. 2015), which (to our knowledge) has not been done before.

The background-subtracted DEMs averaged over the small box along the loop (Fig. 4) are shown in red in Fig. 6. DEMs corresponding to the black box are shown in black, while the background DEMs corresponding to the green box in Fig. 4 are shown in green. The background-subtracted DEMs peak at  $\log(T/K) = 6.2$  for the Maxwellian distribution and  $\kappa = 5$ . The peak of the DEM is shifted to higher  $T$  for  $\kappa = 2-3$ , being at  $\log(T/K) = 6.3$  and  $6.4$  for  $\kappa = 3$  and  $2$ , respectively. This behaviour of the DEMs is mainly the result of the shifts in the ionization equilibrium to higher  $T$ , see Fig. 2 and Mackovjak et al. (2014). The DEMs are multi-thermal, with significant amount of emission originating at temperatures lower than the peak of the DEMs, down to about  $\log(T/K) = 5.9-6.1$ .

The pixel-by-pixel reconstructed  $EM_{\kappa}(T)$  are shown in Fig. 7 for the five temperature bins where the background-subtracted  $DEM_{\kappa}(T)$  is the highest (Fig. 6). Note that the width of the temperature bin is  $\Delta \log(T/K) = 0.1$ . We see that the loop is present in all of these temperature bins. At lower temperatures, it is relatively well-defined, with the  $EM_{\kappa}(T)$  becoming more fuzzy with increasing  $T$  for all  $\kappa$ . This behaviour comes from the emission morphology in the progressively hotter AIA bands.

The DEMs for the Maxwellian distribution and  $\kappa = 5$  contain a spurious high-temperature peak at

$\log(T/K) \geq 7.0$ . This peak is about a factor of  $\approx 30$  weaker than the main one and was reported for on-disk AIA observations also by Dudík et al. (2014c, Sect. 3 therein). This peak is present also in the background DEMs, which may suggest that it is an artifact of the method. The peak gets progressively suppressed with decreasing  $\kappa$ , until it is absent from the background-subtracted DEMs for  $\kappa = 2$ .

We note that in principle, a combination of AIA filter ratios permits diagnostics of  $\kappa$ , but only for isothermal or near-isothermal structures (Dudík et al. 2009; Dzifčáková et al. 2012). This is because such color-color diagram are not monotonic, but contain complicated curves. Since the DEMs obtained are significantly multi-thermal for all  $\kappa$  studied, it is not possible to use the combinations of AIA filter ratios to diagnose  $\kappa$ . Instead, the diagnostic of  $\kappa$  has to be performed using ratios of individual spectral lines that produce monotonic ratio-ratio diagrams (see Sect. 4.3).

#### 4. HINODE/EIS OBSERVATIONS DURING HOP 226

The Extreme-Ultraviolet Imaging Spectrometer (EIS, Culhane et al. 2007) onboard the *Hinode* mission (Kosugi et al. 2007) provides EUV spectra of the Sun in the wavelength ranges 171-212Å and 245-291Å with a spectral resolution of about 22 mÅ and spatial resolution down to 1-2'', corresponding to the width of the slit chosen.

On 2013 March 30, EIS was observing portion of AR 11704 as a part of the Hinode Operation Plan (HOP) 226. HOP 226 was originally designed for diagnostics of non-Maxwellian  $\kappa$ -distributions using weak O IV-O V and S X-S XI lines (see Mackovjak et al. 2013). Since these lines are weak, EIS was rastering an area within the AR core using 2'' slit and long exposures (60s and 600s).



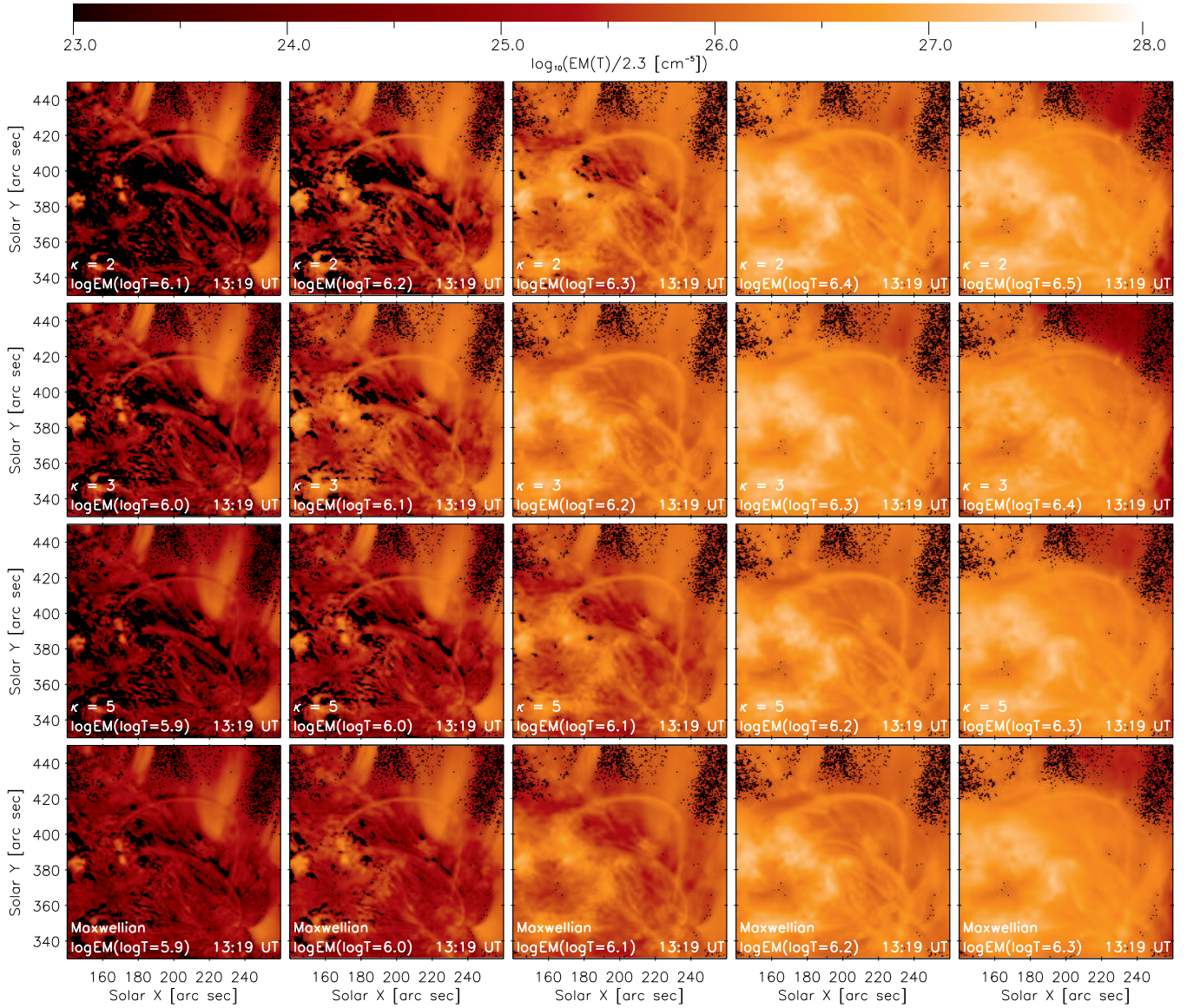


**Figure 7.** Emission measure  $EM_{\kappa}(T)$  at different temperatures  $T$  as a function of  $\kappa$ . The values of  $\kappa$  and  $\log(T/K)$  are indicated at each frame. A color version of this image is available in the online journal.

**Table 1**

Background-subtracted EIS line intensities averaged over the pixels listed. See text for details of the background subtraction. The standard deviations  $\sigma_{10\%}$  and  $\sigma_{20\%}$  are obtained by considering a 10% and 20% calibration uncertainty, respectively. Selfblends are indicated, with very weak transitions in parentheses.

Ion	$\lambda$ [Å]	selfblending transitions [Å]	Loop (288:317)			Loop (300:309)		
			$I$	$\sigma_{10\%}(I)$	$\sigma_{20\%}(I)$	$I$	$\sigma_{10\%}(I)$	$\sigma_{20\%}(I)$
Fe XI	182.167	–	795	99	169	934	117	199
Fe XI	188.216	–	1638	172	332	1947	204	394
Fe XI	257.554	257.538, 257.547, 257.558	398	45	82	414	47	86
Fe XI	257.772	257.725	178	23	38	234	30	50
Fe XII	186.887	186.854, (186.931)	1406	145	283	1498	154	302
Fe XII	195.119	195.179, (195.078), (195.221)	2256	228	453	2506	254	503
Fe XIII	196.525	–	261	27	53	223	23	45
Fe XIII	202.044	–	1346	153	279	1779	202	368
Fe XIII	203.826	203.772, 203.795, 203.835	2591	270	524	2532	264	512

Each 60s and 600s raster contained 10 exposures of the 2'' slit at contiguous positions in Solar X, covering 512'' in Solar Y (heliocentric co-ordinates). For context, as well

as density diagnostics, the raster contained additional lines, notably several strong Fe XI–Fe XIII lines.

Upon examination of the data, we find that the 600s

**Table 2**  
Electron densities diagnosed using individual ratios.

Line ratio	$I_1/I_2$	Loop (288:317)		Loop (300:309)		
		$\log(n_e)_{\text{Maxw.}}$	$\log(n_e)_{\kappa=2}$	$\log(n_e)_{\text{Maxw.}}$	$\log(n_e)_{\kappa=2}$	
Fe XI 182.167 / 188.215	0.49	$9.45^{+0.06}_{-0.10}$	$9.34^{+0.12}_{-0.20}$	0.48	$9.43^{+0.06}_{-0.10}$	$9.32^{+0.12}_{-0.19}$
Fe XII (186.854+186.887) / (195.119+195.179)	0.62	$9.86^{+0.09}_{-0.08}$	$9.83^{+0.03}_{-0.09}$	0.60	$9.79^{+0.10}_{-0.08}$	$9.76^{+0.09}_{-0.02}$
Fe XIII 196.525 / 202.044	0.19	$9.30^{+0.11}_{-0.11}$	$9.20^{+0.15}_{-0.15}$	0.13	$9.12^{+0.12}_{-0.12}$	$9.02^{+0.15}_{-0.16}$
Fe XIII (203.826 sbl) / 202.044	1.92	$9.35^{+0.10}_{-0.10}$	$9.27^{+0.13}_{-0.14}$	1.42	$9.16^{+0.10}_{-0.10}$	$9.08^{+0.13}_{-0.14}$
adopted value		9.0 – 9.5			8.8 – 9.6	

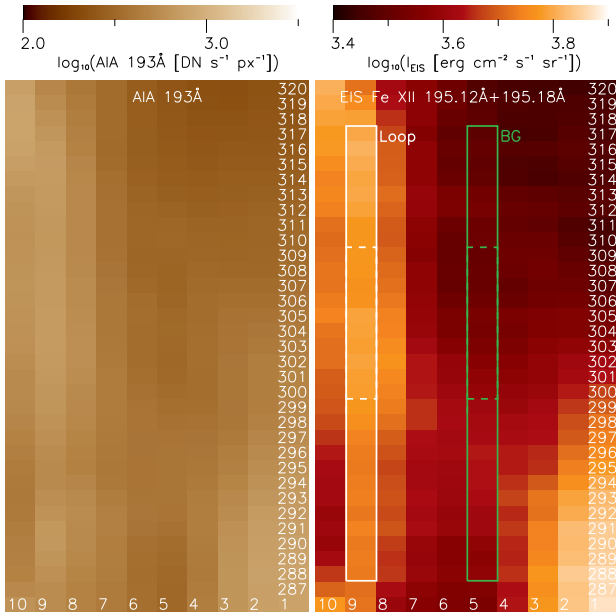


**Figure 8.** A portion of the EIS raster selected for analysis, corresponding to the field of view shown by white box in Fig. 4. Numbers give the pixel coordinates in the raster. *Left:* AIA 193Å pseudo-raster corresponding to the EIS FOV. *Right:* EIS intensities of the Fe XII 195.12Å + 195.18Å selfblend. Pixel size is  $2'' \times 1''$ . A color version of this image is available in the online journal.

rasters suffer badly from an accumulation of cosmic rays, and that the weak O and S lines do not have sufficient intensities for diagnostics. However, the last 60 s raster, starting at 13:11 UT and progressively rastering in the West–East direction, captures a portion of the coronal loop in its ninth exposure at 13:19 UT (position 9 in Fig. 8), with the portion of the loop lying directly along the EIS slit. Some of the O and S lines proposed for diagnostics are again too weak in this 60s exposure. Nevertheless, the strong Fe XI–Fe XIII lines (Table 1) are sufficient to perform diagnostics of the  $\kappa$ -distributions. It is these data that are analyzed here.

#### 4.1. EIS Data Processing and Calibration

We first performed coalignment of the raster with the AIA data. To do this, we use the Fe XII 195.119Å selfblend (hereafter, “195.119Å sbl”) and the AIA 193Å data uncorrected for solar differential rotation, but with removed stray light (Poduval et al. 2013). These AIA data are used to build an AIA 193Å pseudo-raster image by extracting the EIS field of view during each exposure within the raster, averaging individual AIA 193Å frames within the duration of each raster exposure, and convolv-

ing with the EIS point-spread function, which is assumed to be a Gaussian with FWHM of  $2''$  in both  $X$  and  $Y$  directions (Del Zanna et al. 2011b, Appendix A therein). By comparing this AIA 193Å pseudo-raster image with the EIS 195.119Å sbl, we found shifts in the EIS positioning of  $\Delta X = 13''$  and  $\Delta Y = -9.5''$  with respect to AIA. Furthermore, the EIS slit is found to be rotated by  $+1^\circ$  with respect to the Solar  $Y$ . Note that since the EIS raster has only 10 exposures in Solar  $X$ , the EIS raster image cannot be rotated. Rather, the AIA data have to be rotated by  $-1^\circ$  before constructing the AIA 193Å pseudo-raster image. Because of the relative rotation between the two instruments, as well as for simplicity, the positions of the individual EIS pixels will be given in pixel units  $x$  and  $y$  rather than Solar  $X$  and  $Y$ .

The EIS data were calibrated using the standard *eis\_prep.pro* routine available within the SolarSoft platform running under the Interactive Data Language (IDL). During the calibration, the latest in-flight radiometric calibration of Del Zanna (2013a) was used. The calibrated data contain intensities in physical units [ $\text{erg cm}^{-2} \text{s}^{-1} \text{sr}^{-1} \text{Å}^{-1}$ ] and the  $1\text{-}\sigma$  errors on the observed intensities at each spatial and wavelength pixel. The intensities and uncertainties are stored in the separate files, with the error file also containing flags for missing pixels (dusty, hot, warm pixels and pixels affected by cosmic rays). We note that usually, these missing pixels are interpolated during the calibration procedure. However, the number of missing pixels in the raster is relatively high, up to 30%. This brings up concerns about uncertainties in the fitting of the observed intensities at each single spatial pixel (Young 2010).

In this work, the pixels flagged as missing were interpolated only for purposes of visualising the raster field of view containing the loop (Fig. 8, *right*). The missing pixels were excluded from any further analysis, since they cannot always be interpolated with accuracy due to their high number. Instead, we rely on intensities obtained by averaging along a selected loop segment observed in position 9 of the EIS slit. The intensity averaging is done over  $y$  at each wavelength pixel using exclusively pixels not flagged as missing. The same is done at position 5 of the EIS slit, which we chose to represent the background. We selected two loop segments over which the averaging is performed. The first one consists of pixels  $y = 288$  to 317, denoted simply as “loop (288:317)”, and representing the average loop spectrum. The second one is much shorter, consisting of pixels  $y = 300$  to 309, denoted as “loop (300:309)”, and representing a much shorter segment of the loop. We chose to average over longer rather than shorter loop segments in order to minimize errors from photon noise. We also note that the effective EIS

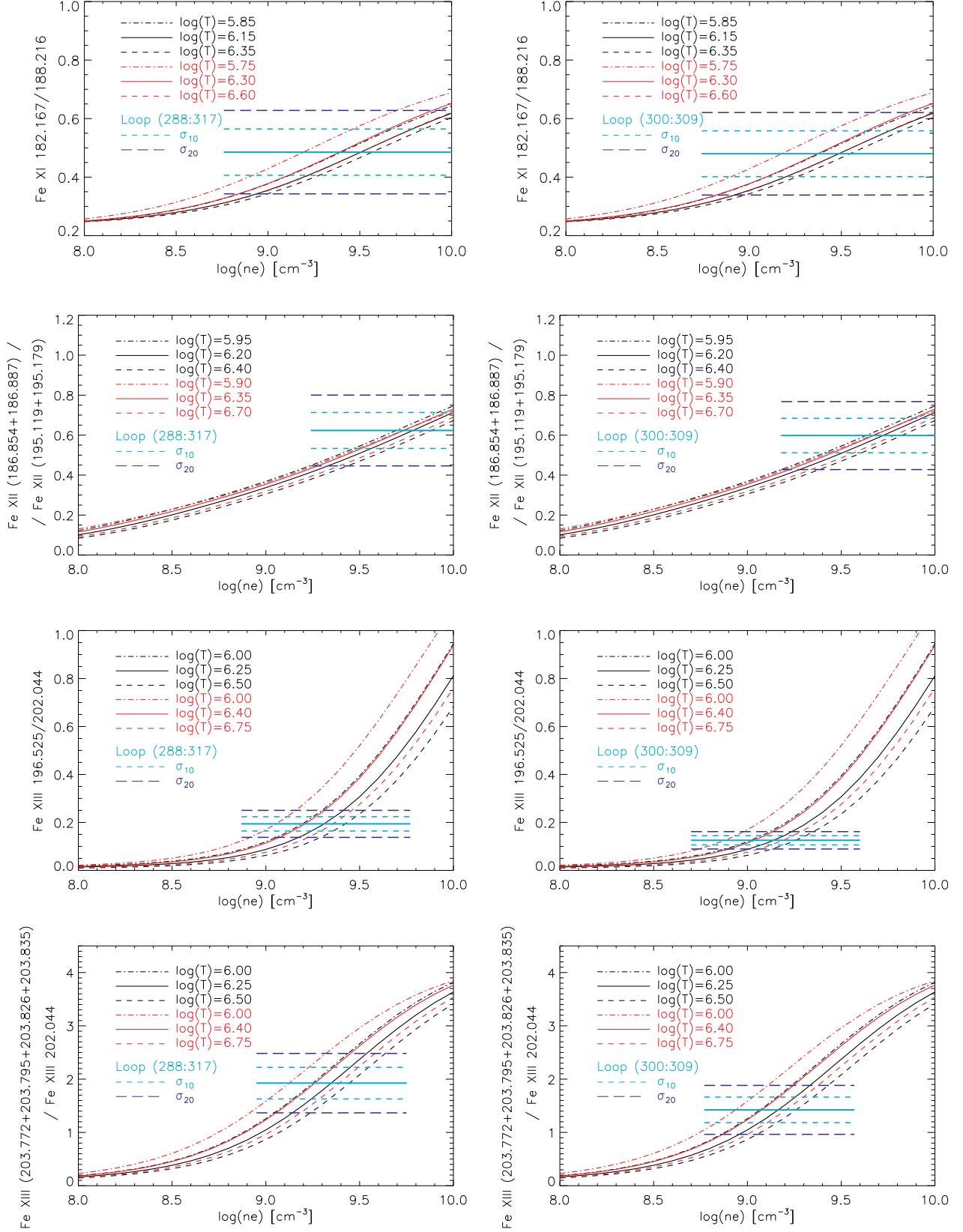


**Figure 9.** Diagnostics of density using Fe XI, Fe XII, and Fe XIII ratios. Black color corresponds to the Maxwellian distribution; red stands for  $\kappa = 2$ . Different line styles correspond to different  $T$  for each distribution (see Dudík et al. (2014b), Figs. 5–7 therein): Full lines stand for the temperature corresponding to the peak of the ion abundance, dashed and dot-dashed lines for the temperatures at which the relative ion abundance is 1% of its maximum. Observed value of the ratio is plotted as the full cyan line. Uncertainties including calibration uncertainties are plotted for illustration. A color version of this image is available in the online journal.

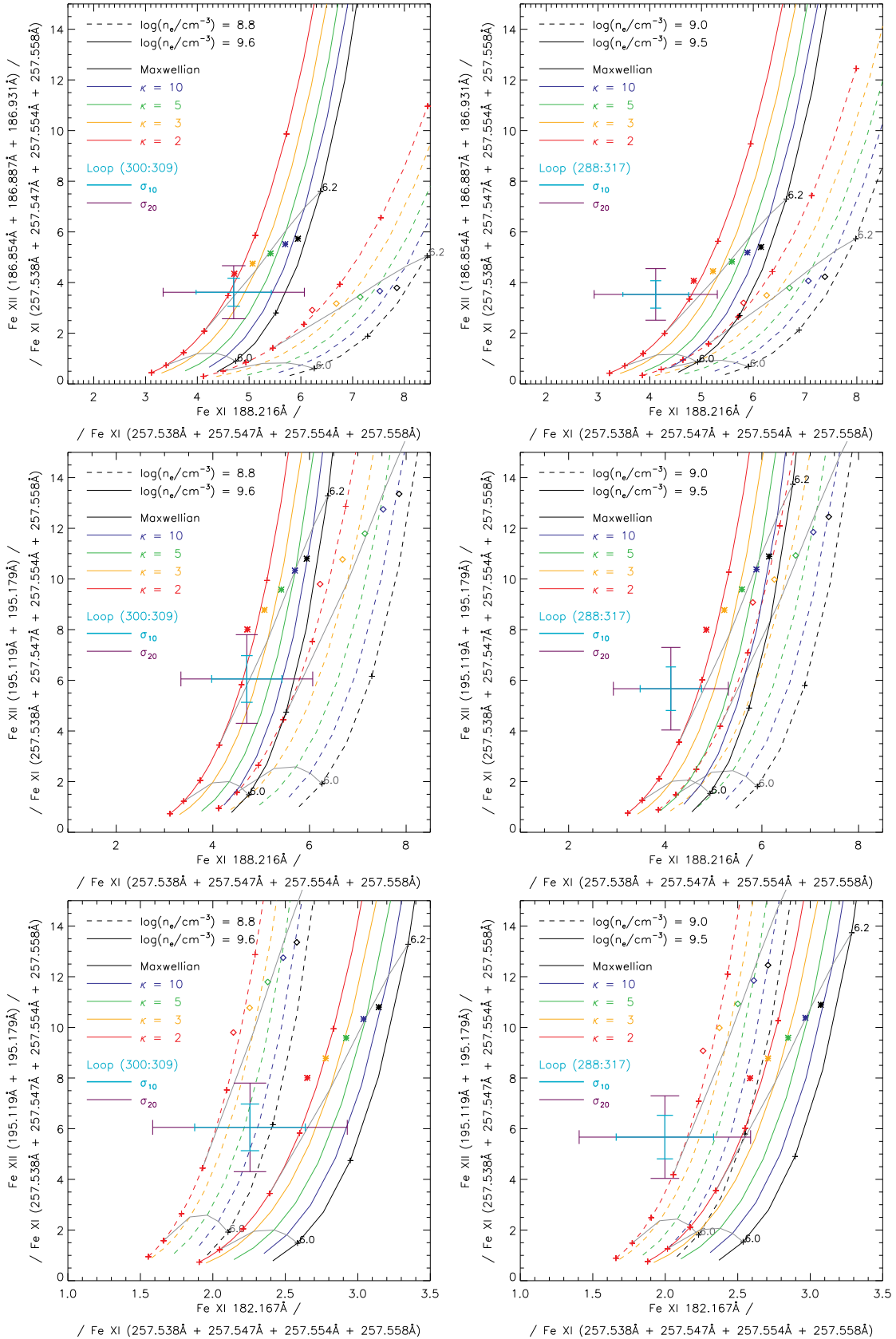


**Figure 10.** Diagnostics of  $\kappa$  involving the Fe XI 257.554 Å selfblend. Different colors correspond to different  $\kappa$ , linestyles denote electron density. Diamonds and asterisks denote the predicted ratios based on DEM analysis. A color version of this image is available in the online journal.

resolution in  $y$  is only about  $3''$ – $4''$  because of the instru-

ment point-spread function.

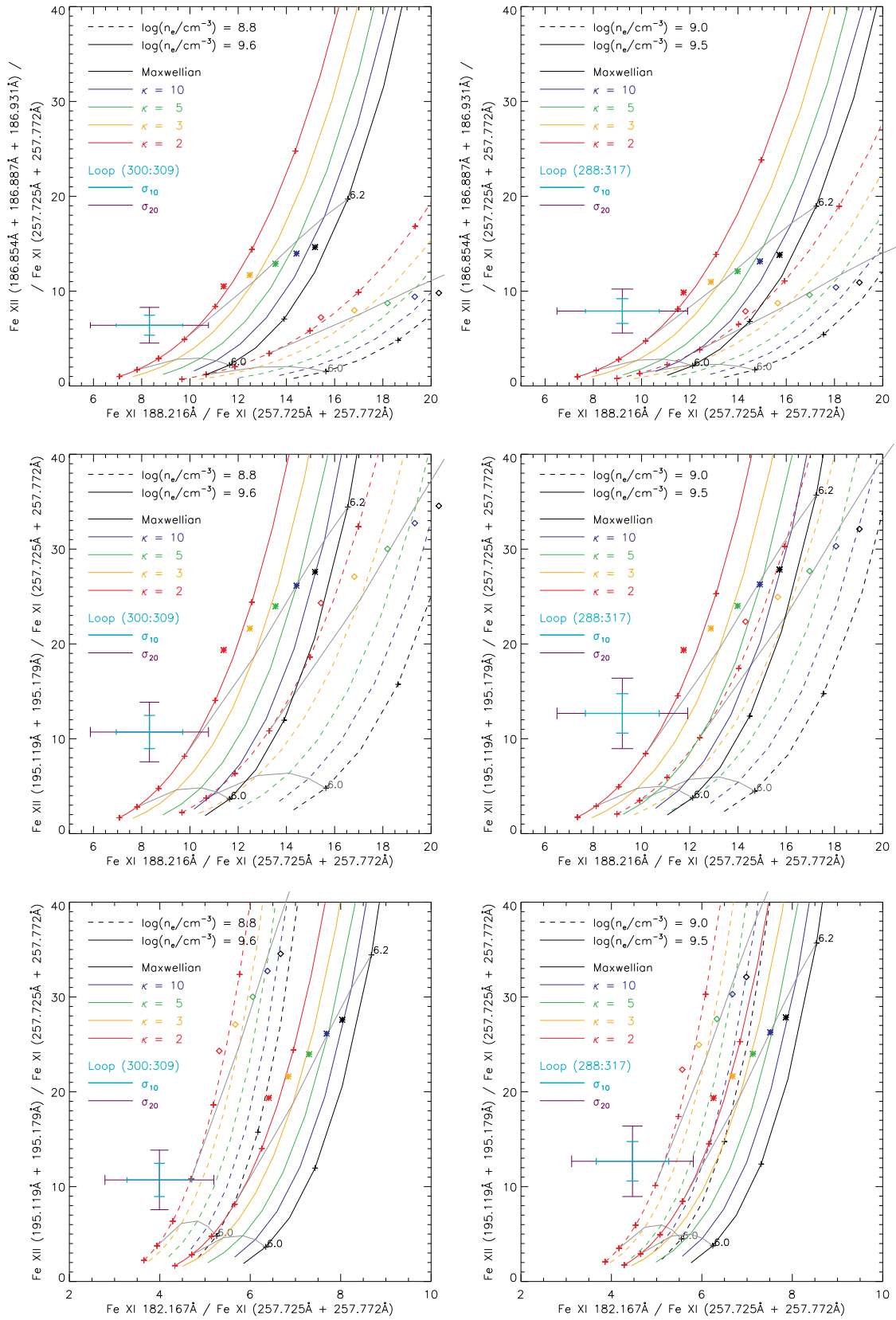


**Figure 11.** Diagnostics of  $\kappa$  involving the Fe XI 257.772 Å selfblend. Different colors correspond to different  $\kappa$ , linestyles denote electron density. Diamonds and asterisks denote the predicted ratios based on DEM analysis. A color version of this image is available in the online journal.

Subsequently, the average spectrum of the background at position 5 is subtracted from the average loop spectrum. The resulting background-subtracted loop spectrum is fitted with Gaussian line profiles and locally linear continua, taking into account known blends and self-blends (e.g., Del Zanna 2010, 2011, 2012; Dudík et al. 2014b). The intensities obtained are listed in Table 1. The uncertainties on these intensities are obtained by error propagation of the uncertainties of the photon noise and dark-current subtraction that are the output of the *eis\_prep.pro*. These uncertainties are then added in quadrature with the uncertainty of the EIS radiometric calibration. We consider two values of the radiometric calibration uncertainty, 10% and 20%. The 20% uncertainty is the uncertainty of the ground calibration (Culhane et al. 2007), while Wang et al. (2011) argues that the in-flight uncertainty is smaller, about 10%. The final uncertainties on the line intensities are denoted  $\sigma_{10\%}$  and  $\sigma_{20\%}$ , respectively, and are also listed in Table 1.

We note that we employed the revised radiometric calibration of Del Zanna (2013a) rather than the ground calibration (Culhane et al. 2007) or the calibration of Warren et al. (2014). Del Zanna (2013a) showed that significant departures from the EIS ground calibration occurred over time, especially with the lines in the long-wavelength channel of EIS being underestimated by about a factor of two for observations after 2010. Line ratios were used to obtain a calibration corrected for decrease of sensitivity. Warren et al. (2014) obtained similar results, comparing the EIS radiances from the whole Sun with the *SDO/EVE* irradiances together with the quiet-Sun DEM modeling. However, the *EVE* calibration can be an additional source of uncertainty. Furthermore, the quiet-Sun DEM modelling used by Warren et al. (2014) can in itself be sensitive to  $\kappa$  (Mackovjak et al. 2014), which could entangle the calibration to diagnostics and overcomplicate the problem. The Del Zanna (2013a) calibration is sufficient for our purposes, as the diagnostics of electron density (Sect. 4.2) as well as the diagnostics of  $\kappa$  (Sect. 4.3) rely only on line ratios (Dzifčáková & Kulinová 2010; Mackovjak et al. 2013; Dudík et al. 2014b), and thus do not require absolute calibration.

We also note that the decrease of sensitivity of the long-wavelength channel of EIS by about a factor of 2 is clearly significant for our diagnostic purposes. This is because the diagnostics of  $\kappa$  in Sect. 4.3 involve lines from both the short-wavelength and long-wavelength EIS channels. We note that the Del Zanna (2013a) calibration applies only to observations up to September 2012, therefore we have assumed that no further degradation occurred since. If the long-wavelength channel sensitivity further degraded significantly, the radiances of the long-wavelength channel would be underestimated, and the ratios shown in Figs. 10–12 would decrease.

#### 4.2. Density Diagnostics

Diagnostics of electron density are a necessary prerequisite to diagnostics of  $\kappa$  (Sect. 4.3). The Fe lines observed by EIS (Table 1) contain several combinations of lines sensitive to electron density (e.g., Watanabe et al. 2009; Young et al. 2009; Del Zanna 2010, 2011; Del Zanna et al. 2012b; Dudík et al. 2014b). The density-sensitive line ratios are listed in Table 2,

where the diagnosed densities are also listed.

The diagnostics of density are performed using the method developed first by Dzifčáková & Kulinová (2010). The theoretical line ratios were calculated by Dudík et al. (2014b) using the latest available atomic data (see also Sect. 2.2). This density diagnostics method employs ratios of lines arising in the same ion. The sensitivity of these ratios to  $n_e$  cannot be significantly influenced by their sensitivity to  $T$  and  $\kappa$ , otherwise the density diagnostics would be precluded. Typically, it was found that density-sensitive ratios commonly used for the Maxwellian distribution can be used under the assumption of  $\kappa$ -distributions in the same manner, albeit the resulting densities can be up to 0.1 dex lower for  $\kappa = 2$  (red color in Fig. 9). This uncertainty due to the unknown value of  $\kappa$  is however comparable or smaller than the uncertainty due to the dependence of individual ratios on  $T$  (Dzifčáková & Kulinová 2010; Mackovjak et al. 2013; Dudík et al. 2014a,b). The overall uncertainty due to the a-priori unknown values of  $T$  and  $\kappa$  can be in some instances as large as 0.4 dex in  $\log(n_e/\text{cm}^{-3})$  (e.g., Fig. 9).

In principle, calibration uncertainties compound the uncertainty of the diagnosed density. However, the EIS density-sensitive lines belonging to the same ion have typically similar wavelengths, and are all observed within the same EIS channel. It is unlikely for the corresponding line ratios to be severely affected by calibration uncertainties. Therefore, we chose to ignore the calibration uncertainties when diagnosing the electron density. Nevertheless, for illustration, the values of individual ratios derived from the background-subtracted observations (Sect. 4.1) are plotted in Fig. 9 together with their uncertainties.

The densities diagnosed using the Fe XI and Fe XIII ratios are consistent within their respective errors (Fig. 9, Table 2). However, the densities diagnosed using Fe XII are higher by about 0.5 dex compared to those diagnosed using Fe XIII. I.e., given the densities diagnosed using Fe XI and Fe XIII, the calibrated intensities of the Fe XII 186.887Å selfblend seem to be too high compared to the intensities of the Fe XII 195.119Å sbl by about 20–30%. The reason for this discrepancy is unknown. Del Zanna et al. (2012b) showed that the new atomic model for Fe XII provides significantly lower densities than the previous model, by about 0.4 dex. The previous model consistently provided values much higher than those obtained from Fe XI and Fe XIII (see, e.g., Young et al. 2009). The densities obtained for the background-subtracted intensities from Fe XII are much reduced using the new atomic data of Del Zanna et al. (2012b), but still higher by about 0.5 dex than those obtained here from Fe XI and Fe XIII. The discrepancy is lower when background-subtraction is ignored. The reason is unclear despite the fact that we use here the same atomic data and calibration as Del Zanna et al. (2012b) and Del Zanna (2013a). Nevertheless, the intensity of the 186.887Å line is somewhat suspect since the shape of the EIS effective area curve in the Del Zanna (2013a) calibration differs from that of the ground calibration (see Fig. 8 *top* therein), or from that of Warren et al. (2014, Fig. 7 therein). The differences are of the order of several tens of per cent, which is comparable to

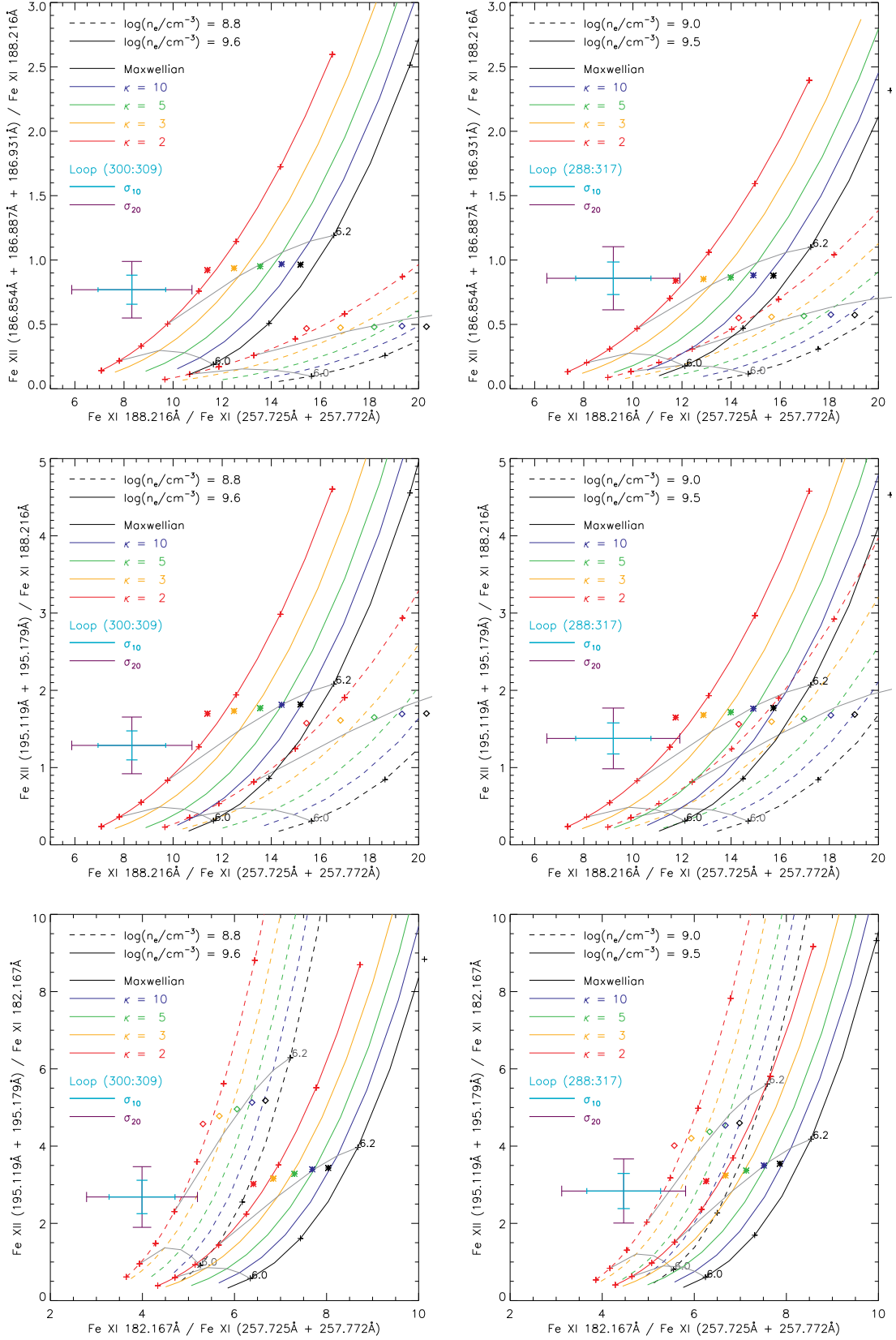


**Figure 12.** Diagnostics of  $\kappa$  involving the Fe XI 257.772Å selfblend and Fe XII / Fe XI ratios using lines only from the EIS short-wavelength channel. Different colors correspond to different  $\kappa$ , linestyles denote electron density. Diamonds and asterisks denote the predicted ratios based on DEM analysis. A color version of this image is available in the online journal.

the 20% calibration uncertainty. We note that changing the Fe XII 186.887Åsbl /195.119Åsbl ratio by about 20% would bring the diagnosed densities into consistency with the Fe XI and Fe XIII ones (Fig. 9). Furthermore, if the 20% calibration uncertainties are taken into account, the observed Fe XII ratio still yields densities consistent with the other ratios, since the lower violet line in Fig. 9 yields densities of  $\log(n_e/\text{cm}^{-3}) = 9.2\text{--}9.4$ .

Additionally, because of the strong overlap of the Fe XI–Fe XIII relative ion abundances (Fig. 2) at temperatures corresponding to the peaks of the background-subtracted DEMs for all  $\kappa$  (Fig. 6), it is unlikely that the diagnosed loop is a multi-density one. If it were, the Fe XIII density-sensitive ratios, which have stronger density sensitivity at  $\log(n_e/\text{cm}^{-3}) = 9.5$ , should be biased towards higher densities more than the Fe XII ratio, whose increase with  $n_e$  is weaker.

For these reasons, we adopt the densities diagnosed using Fe XI and Fe XIII for further analysis. For the average loop spectrum, the diagnosed value is  $\log(n_e/\text{cm}^{-3}) = 9.0\text{--}9.5$ , while for the loop spectrum averaged through pixels  $y = 300\text{--}309$  we obtain the value of  $\log(n_e/\text{cm}^{-3}) = 8.8\text{--}9.6$ . We note that these values are conservative, as they are chosen to contain all the densities diagnosed using Fe XI and Fe XIII together with their respective errors (Table 2).

### 4.3. Diagnostics of $T$ and $\kappa$

#### 4.3.1. Ratio-Ratio Diagrams

Having obtained constraints on the electron density, we can next diagnose  $\kappa$ . A principal constraint is that the diagnostics of  $\kappa$  have to be performed using lines that are also sensitive to temperature. This comes from the nature of the task, as both the excitation as well as ionization and recombination rates are a function of both  $T$  and  $\kappa$ . Typically, line ratios sensitive to  $\kappa$  involve lines populated by different parts of the distribution (Dzifčáková 2006a), i.e., either lines with different behaviour of the excitation cross-section with  $E$ ; or lines with different excitation thresholds  $\Delta E_{ji}$ , i.e., lines formed at different wavelengths; or both. Such line ratios will always be sensitive to temperature as well. Line ratios sensitive to  $\kappa$  are then combined with the line ratios involving lines from neighbouring ions, that are strongly sensitive to  $T$ , but also sensitive to  $\kappa$ .

Furthermore, if the relative level population depends on density,  $\kappa$ -sensitive line ratios belonging to the same ion typically have smaller sensitivity to  $\kappa$  than to  $n_e$ , although exceptions occur (Dzifčáková 2006a; Dzifčáková & Kulinová 2010; Mackovjak et al. 2013; Dudík et al. 2014b). The diagnosed electron density is then used to constrain the diagnostics using the ratio-ratio diagrams (Dzifčáková & Kulinová 2010; Mackovjak et al. 2013).

This is the approach we chose here. From the lines listed in Table 1, Fe XI is the only ion offering strongly temperature-sensitive line ratios. There are four temperature-sensitive ratios of Fe XI lines, each involving a line from the EIS short-wavelength channel (182.167Å or 188.216Å) and a line from the EIS long-wavelength channel (257.554Å sbl or 257.772Å sbl, see Table 1). These Fe XI line ratios are combined with ratios involving a Fe XII line. Both the selfblends at

186.887Å and 195.119Å are used. This is because of the possible calibration problems involving the 186.887Å sbl (Sect. 4.2). The various combinations are shown in Figs. 10, 11 and 12. The observed line ratios together with their uncertainties are shown as large crosses where the azure and violet errorbars are calculated using the  $\sigma_{10\%}$  and  $\sigma_{20\%}$  uncertainties of the individual lines involved, respectively (see Table 1). The calibration uncertainty is included since various ratios involve lines observed in both EIS channels.

The ratio-ratio diagrams involving the 257.554Å sbl (Fig. 10) show strong sensitivity to  $T$  and sensitivity to  $\kappa$  that is of the order of  $\approx 20\%$ . However, the large calibration uncertainties together with the uncertainty in the diagnosed  $\log(n_e/\text{cm}^{-3})$  prevent positive diagnostics using some of these diagrams for both loop segments. This is because the  $1\text{-}\sigma_{20\%}$  errorbar intersects all curves for different  $\kappa$  for at least one of the diagnosed limits on  $\log(n_e/\text{cm}^{-3})$ . The situation is worse for the loop (300:309), where the observed ratios are closer and intersect more curves for different  $\kappa$  on the ratio-ratio diagrams (Fig. 10, *left*) than in the case of the average loop spectrum (loop (288:317), Fig. 10, *right*). For the average loop spectrum, we can diagnose  $\kappa \lesssim 5$  using the ratios involving Fe XI 188.216Å / (Fe XI 257.554Å sbl). This is because for all ratios in Fig. 10, *right*, the red and orange ratio-ratio curves corresponding to  $\kappa = 2$  and 3 intersect all the violet errorbars, while others do not. Nevertheless, the green ratio-ratio curve ( $\kappa = 5$ ) is in close vicinity of the errorbar in the *top right* panel.

The situation is much better when using ratio-ratio diagrams involving the Fe XI 257.772Å selfblend (Fig. 11). Compared to the spread of the curves for individual  $\kappa$  and  $\log(n_e/\text{cm}^{-3})$ , the uncertainty of the observed ratios is smaller, and the observed ratios are located further away from the curves. This permits diagnostics of  $\kappa \lesssim 3$ , a strongly non-Maxwellian distribution. We note that this result is the same whether the Fe XII 186.887Å selfblend or the 195.119Å selfblend is used.

To confirm this diagnostic, in Fig. 12 we substitute the Fe XI 257.772Å sbl by other Fe XI lines in the Fe XII / Fe XI ratio. Again,  $\kappa \lesssim 3$  is found independently of the combination of lines used (Fig. 12), with majority of the ratio-ratio diagrams indicating  $\kappa \lesssim 2$ .

We note that the results of the diagnostics of  $\kappa$  are not dependent on which of the two Fe XII lines is used. Both the Fe XII 186.887Å and 195.119Å selfblends yield similar results in terms of  $\kappa$  (Figs. 10–12). This allows us to establish confidence in using the Fe XII lines to diagnose  $\kappa$  despite the possible calibration problems mentioned in Sect. 4.2.

Finally, we point out that the loop evolution as observed by AIA (Sect. 3.2) is unlikely to strongly affect the diagnostics of  $\kappa$ . This is because the AIA 193Å intensities (dominated by Fe XII; Del Zanna 2013b) do not change by more than 1–2% during the EIS observations at 13:19 UT (Fig. 5, *top*).

#### 4.3.2. Influence of the DEM on Diagnostics of $\kappa$

Originally, the ratio-ratio diagrams were developed for simultaneous diagnostics of  $T$  and  $\kappa$  based on the assumption that the observed structure is isothermal (Dzifčáková & Kulinová 2010; Mackovjak et al. 2013).



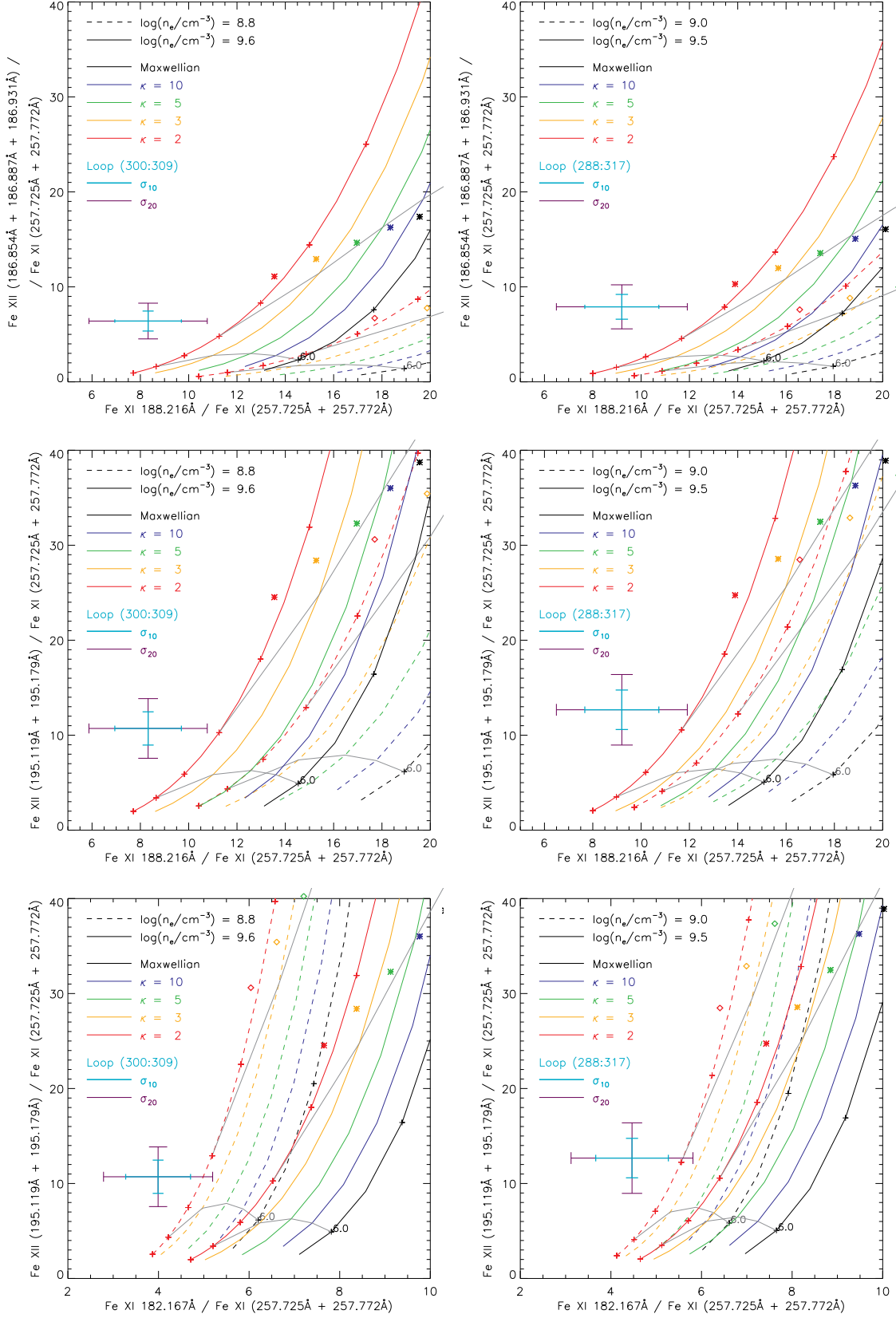


**Figure 13.** Same as Fig. 11, but with atomic data corresponding to CHIANTI 7.1 and the KAPPA package. A color version of this image is available in the online journal.

The results presented for the transient loop in Sect. 3.3 however suggest that the loop is multi-thermal independently of the value of  $\kappa$ . Therefore, we investigated the influence of DEM on the diagnostics of  $\kappa$ .

Unfortunately, the EIS raster obtained during HOP 226 does not contain enough strong lines for determination and constraining the DEM, especially throughout the entire  $\log(T/K) = 5.5 - 7.0$  range. Therefore, we use the AIA data to perform the DEM diagnostics and note that Del Zanna (2013b) showed that the AIA observations can be used to predict the EIS radiances to within the calibration uncertainties of both instruments. Although these authors used preferentially a DEM reconstruction technique different from the Hannah & Kontar (2012) one that is used here (Sect. 3.3), the Hannah & Kontar (2012) technique was also tested by Del Zanna (2013b) and a reasonable agreement was found.

First, we produce an AIA pseudo-raster for each AIA band similar to that shown in Fig. 8, *left*. Subsequently, the DEM is derived using the technique of Hannah & Kontar (2012, 2013) similarly as in Sect. 3.3 for each pixel of these AIA pseudo-rasters. We perform the averaging of the DEMs the same way as for the EIS raster (i.e., over pixels at position 9 corresponding to the loop,  $y = 288-317$  and  $300-309$ ), subtract the background at position 5, and then use these background-subtracted DEMs to predict the intensities of individual EIS Fe XI–Fe XIII lines.

The predicted ratios of individual lines are shown as a function of  $\kappa$  on each of the ratio-ratio diagrams in Figs. 10–12. Diamonds are used for the diagnosed lower limits on  $\log(n_e/\text{cm}^{-3})$  (Sect. 4.2), asterisks for the upper limits. Generally, the predicted ratios for each  $\kappa$  are located close to the corresponding curves, indicating that these curves can still be used to indicate the value of  $\kappa$  in the observed plasma even if this plasma is multi-thermal. Furthermore, we find that *with decreasing  $\kappa$ , the predicted ratios converge on the observed values in all cases*, indicating that the plasma is strongly non-Maxwellian with  $\kappa \lesssim 2$ . This is so even for the cases when the isothermal ratio-ratio diagrams cannot be used to constrain the value of  $\kappa$ , such as the Fe XI  $188.216\text{\AA} / (\text{Fe XI } 257.554\text{\AA} \text{ sbl}) - (\text{Fe XII } 186.887\text{\AA} \text{ sbl}) / (\text{Fe XI } 257.554\text{\AA} \text{ sbl})$  in Fig. 10, *middle row*, or the similar combination with Fe XII  $195.119\text{\AA} \text{ sbl}$  in Fig. 10, *bottom row*.

## 5. ATOMIC DATA UNCERTAINTIES

The atomic datasets for astrophysical spectroscopy are always incomplete, since they contain only a finite number of energy levels and the corresponding transitions. Therefore, we investigated the influence of the atomic data uncertainties on the analysis presented here. To do that, we repeated the analysis presented in Sect. 4 using older atomic data that are available in the CHIANTI, version 7.1 (Dere et al. 1997; Landi et al. 2013). The calculations for the Maxwellian distribution were performed using CHIANTI v7.1 and the corresponding calculations for the  $\kappa$ -distributions were performed using the KAPPA package (Dzifčáková et al. 2015).

The density diagnostics performed in Sect. 4.2 using Fe XI and Fe XIII ratios remain valid, since these density-

sensitive ratios do not change appreciably (see Figs. 5 and 7 in Dudík et al. 2014b) even if the individual line intensities change by up to  $\approx 20\%$ . Therefore, the conservative densities adopted (Table 2) are kept.

Examples of the diagnostics of  $\kappa$ , including the effect of DEM using the older atomic data, are presented in Fig. 13, which shows ratios involving the Fe XI  $257.772\text{\AA}$  selfblend. These diagrams correspond to those shown in Fig. 11 for the newest atomic data. From Fig. 13 we see that the diagnostics of  $\kappa \lesssim 2$  remain valid even if older atomic data are used.

We note that the newest atomic data of Del Zanna (2010), Del Zanna (2011), Del Zanna et al. (2012b), and Del Zanna & Storey (2013) used in Sects. 2–4 represent significant improvement over the previous ones, especially in the case of Fe XII, where differences of up to 60% in intensities of key lines were found (Del Zanna et al. 2012b), including the  $195.119\text{\AA}$  selfblend. We find similar increases found for all  $\kappa$ . The Fe XI line intensities are found to be increased for all  $\kappa$  by about 10–20%, although details depend on  $\kappa$  and the particular line. These increases in line intensities are due to the increased contribution from resonances as well as cascading from the  $n = 4$  level (Del Zanna et al. 2012a,b; Del Zanna & Storey 2013) and cause the change in the theoretical ratio-ratio diagrams (compare Fig. 11 with Fig. 13).

Finally, we note that the newest atomic data used in Sects. 2–4 do not include contributions from the  $n \geq 5$  levels. For Fe XI, the contributions of cascading from  $n \geq 5$  to Fe XI line intensities are about 10–20% (Del Zanna & Storey 2013). For the transitions from the  $3s^2 3p^2 3d$  configuration in Fe XII (i.e., the  $186.887\text{\AA}$  and  $195.119\text{\AA}$  lines), the missing contributions from cascading is smaller, of the order of 5% only (Del Zanna et al. 2012b). Including these contributions would move the diagnostic diagrams (Fig. 10–12) down in the  $y$ -direction. Therefore, more complete atomic data are unlikely to change the results of the diagnostics of  $\kappa$ .

## 6. SUMMARY

We reported on imaging and spectroscopic observations of a transient coronal loop observed within the core of AR 11704 on 2013 March 30. The loop reappeared in the same location as the already faded flare arcade of the B8.9-class microflare peaking about three hours earlier. The transient loop persisted for nearly two hours, during which it evolved into a series of individual threads. By examining the AIA data, we found no signatures of hot, flare-like emission being associated with the loop. These results were confirmed using the DEM reconstruction by the regularized inversion method of Hannah & Kontar (2012) and Hannah & Kontar (2013), showing the relative absence of hot plasma except a spurious peak that is also present in the background. This method was employed in conjunction with the AIA responses emission calculated for the  $\kappa$ -distributions by Dzifčáková et al. (2015). We found that the loop is multi-thermal for all  $\kappa$  considered, with the DEMs peaking at  $\log(T/K) = 6.3$  for the Maxwellian distribution, and at 6.5 for  $\kappa = 2$ . The spurious high-temperature peak becomes less prominent with decreasing  $\kappa$ , and it disappears for  $\kappa = 2$ .

We analyzed the spectroscopic data obtained by *Hin-*

ode/EIS in order to perform diagnostics of density and  $\kappa$ . Several density-sensitive ratios of Fe XI, Fe XII and Fe XIII were used in conjunction with the latest EIS calibration and the latest available atomic data. We find consistency between the densities diagnosed from the background-subtracted Fe XI and Fe XIII intensities, with the Fe XII intensities yielding higher densities. However, the density-diagnostics using Fe XII may still be consistent with the Fe XI and Fe XIII ones if the EIS calibration uncertainty is taken into account. Using Fe XI and Fe XIII yields a conservative estimate of electron density of the order of  $\log(n_e/\text{cm}^{-3}) = 8.8\text{--}9.6$  for a loop segment  $10''$  long, and  $\log(n_e/\text{cm}^{-3}) = 9.0\text{--}9.5$  for the average spectrum of the loop along position 9 of the EIS slit.

This diagnosed electron density is then used to constrain the diagnostic of  $\kappa$ . To do that, we use the temperature-sensitive ratios involving Fe XI lines from both EIS detectors in combination with the ratios involving Fe XII and Fe XI lines. We found that ratios involving the Fe XI 257.554Å selfblend can preclude a successful diagnostic due to the calibration uncertainty being larger than the spread of the curves for individual  $\kappa$ . However, all ratios involving the Fe XI 257.772Å selfblend together with other Fe XI and Fe XII lines consistently yield  $\kappa \lesssim 2$ , i.e., an extremely non-Maxwellian situation.

We next studied the influence of the plasma multithermality on the diagnostics of  $\kappa$ . Since the EIS data are insufficient to obtain the DEMs, we obtained the DEMs from the AIA data. These DEMs were used to predict the EIS line intensities as a function of  $\kappa$ . We found that, with decreasing  $\kappa$ , all ratios of the predicted Fe line intensities converge on the observed values. These results confirm the diagnosed value of  $\kappa = 2$  and provide first quantitative description of the non-Maxwellian distribution of electron energies in a coronal loop.

We note that the transient loop studied here is not a typical coronal loop. This is due to its rather low temperature compared to typical active region cores, the ongoing magnetic reconnection as evidenced by the brightenings and jetting activity near its right footpoint, as well as its appearance in the same spatial location as the previous B8.9-class microflare. Nevertheless, the results presented here demonstrate the viability of the methods for diagnostics of  $\kappa$ . Such methods should be applied in the future on the analysis of typical, well-defined coronal loops to search for possible signatures of impulsive heating.

Finally, we note that the 20% calibration uncertainty, typical of the EUV spectroscopic instrumentation, can represent a severe limitation to the diagnostics of non-Maxwellian distribution. Such large calibration uncertainty contributes to the possible mis-interpretation of the observations, as it is always possible to obtain *some* temperatures and DEMs, if a diagnostic of  $\kappa$  is not performed. Decreasing the calibration uncertainty to about 10% would significantly contribute to enabling the diagnostics of non-Maxwellian distributions from EUV spectra.

The authors thank the referee for comments leading to the improvement of the manuscript. The authors are also grateful to Dr. Iain Hannah for the availability of

the regularized inversion method for reconstructing the DEMs. JD acknowledges support from the Royal Society via the Newton Fellowships Programme. JD, EDZ, ŠM, PK, and FF acknowledges the support by Grant Agency of the Czech Republic, Grant No. P209/12/1652. ŠM also acknowledges Comenius University Grant No. UK/620/2014. GDZ and HEM acknowledge STFC. The atomic data were calculated within the UK APAP network, funded by STFC. The authors also acknowledge the support from the International Space Science Institute through its International Teams program. Hinode is a Japanese mission developed and launched by ISAS/JAXA, with NAOJ as domestic partner and NASA and STFC (UK) as international partners. It is operated by these agencies in cooperation with ESA and NSC (Norway). AIA data are courtesy of NASA/SDO and the AIA science team. CHIANTI is a collaborative project involving the NRL (USA), RAL (UK), MSSL (UK), the Universities of Florence (Italy) and Cambridge (UK), and George Mason University (USA).

## REFERENCES

- Aulanier, G., Janvier, M., & Schmieder, B. 2012, *A&A*, 543, A110  
Aulanier, G., Pariat, E., Démoulin, P., & DeVore, C. R. 2006, *Sol. Phys.*, 238, 347  
Aulanier, G., Golub, L., DeLuca, E. E., et al. 2007, *Science*, 318, 1588  
BenMoussa, A., Gissot, S., Schühle, U., et al. 2013, *Sol. Phys.*, 288, 389  
Bian, N. H., Emslie, A. G., Stackhouse, D. J., & Kontar, E. P. 2014, *ArXiv e-prints*  
Boerner, P., Edwards, C., Lemen, J., et al. 2012, *Sol. Phys.*, 275, 41  
Bradshaw, S. J., Klimchuk, J. A., & Reep, J. W. 2012, *ApJ*, 758, 53  
Burge, C. A., MacKinnon, A. L., & Petkaki, P. 2014, *A&A*, 561, A107  
Burge, C. A., Petkaki, P., & MacKinnon, A. L. 2012, *Sol. Phys.*, 280, 575  
Cargill, P. J., Vlahos, L., Baumann, G., Drake, J. F., & Nordlund, Å. 2012, *Space Sci. Rev.*, 173, 223  
Collier, M. R. 2004, *Advances in Space Research*, 33, 2108  
Collier, M. R., Hamilton, D. C., Gloeckler, G., Bochsler, P., & Sheldon, R. B. 1996, *Geophys. Res. Lett.*, 23, 1191  
Culhane, J. L., Harra, L. K., James, A. M., et al. 2007, *Sol. Phys.*, 243, 19  
De Pontieu, B., Title, A. M., Lemen, J. R., et al. 2014, *Sol. Phys.*  
Del Zanna, G. 2010, *A&A*, 514, A41  
— 2011, *A&A*, 533, A12  
— 2012, *A&A*, 537, A38  
— 2013a, *A&A*, 555, A47  
— 2013b, *A&A*, 558, A73  
Del Zanna, G., Mitra-Kraev, U., Bradshaw, S. J., Mason, H. E., & Asai, A. 2011a, *A&A*, 526, A1  
Del Zanna, G., O’Dwyer, B., & Mason, H. E. 2011b, *A&A*, 535, A46  
Del Zanna, G., & Storey, P. J. 2012, *A&A*, 543, A144  
— 2013, *A&A*, 549, A42  
Del Zanna, G., Storey, P. J., Badnell, N. R., & Mason, H. E. 2012a, *A&A*, 541, A90  
— 2012b, *A&A*, 543, A139  
— 2014, *A&A*, 565, A77  
Dere, K. P., Landi, E., Mason, H. E., Monsignori Fossi, B. C., & Young, P. R. 1997, *A&AS*, 125, 149  
Dudík, J., Del Zanna, G., Dzifčáková, E., Mason, H. E., & Golub, L. 2014a, *ApJ*, 780, L12  
Dudík, J., Del Zanna, G., Mason, H. E., & Dzifčáková, E. 2014b, *A&A*, in press  
Dudík, J., Janvier, M., Aulanier, G., et al. 2014c, *ApJ*, 784, 144  
Dudík, J., Kulínová, A., Dzifčáková, E., & Karlický, M. 2009, *A&A*, 505, 1255

- Dzifčáková, E. 2002, *Sol. Phys.*, 208, 91  
 —. 2006a, *Sol. Phys.*, 234, 243  
 Dzifčáková, E. 2006b, in *ESA Special Publication*, Vol. 617, SOHO-17. 10 Years of SOHO and Beyond  
 Dzifčáková, E., & Dudík, J. 2013, *ApJS*, 206, 6  
 Dzifčáková, E., Dudík, J., & Karlický, M. 2012, in *Astronomical Society of the Pacific Conference Series*, Vol. 456, Fifth Hinode Science Meeting, ed. L. Golub, I. De Moortel, & T. Shimizu, 135  
 Dzifčáková, E., & Kulínová, A. 2010, *Sol. Phys.*, 263, 25  
 —. 2011, *A&A*, 531, A122  
 Dzifčáková, E., & Mason, H. E. 2008, *Sol. Phys.*, 247, 301  
 Dzifčáková, E. 1992, *Sol. Phys.*, 140, 247  
 Dzifčáková, E., Dudík, J., Kotrč, P., Fárník, F., & Kulínová, A. 2015, *ApJS*  
 Feldman, U., Landi, E., & Doschek, G. A. 2007, *ApJ*, 660, 1674  
 Gordovskyy, M., Browning, P. K., Kontar, E. P., & Bian, N. H. 2013, *Sol. Phys.*, 284, 489  
 —. 2014, *A&A*, 561, A72  
 Hannah, I. G., Hudson, H. S., Hurford, G. J., & Lin, R. P. 2010, *ApJ*, 724, 487  
 Hannah, I. G., & Kontar, E. P. 2012, *A&A*, 539, A146  
 —. 2013, *A&A*, 553, A10  
 Hasegawa, A., Mima, K., & Duong-van, M. 1985, *Physical Review Letters*, 54, 2608  
 Klimchuk, J. A. 2006, *Sol. Phys.*, 234, 41  
 Klimchuk, J. A., Karpen, J. T., & Antiochos, S. K. 2010, *ApJ*, 714, 1239  
 Kosugi, T., Matsuzaki, K., Sakao, T., et al. 2007, *Sol. Phys.*, 243, 3  
 Laming, J. M., & Lepri, S. T. 2007, *ApJ*, 660, 1642  
 Landi, E., Young, P. R., Dere, K. P., Del Zanna, G., & Mason, H. E. 2013, *ApJ*, 763, 86  
 Le Chat, G., Issautier, K., Meyer-Vernet, N., & Hoang, S. 2011, *Sol. Phys.*, 271, 141  
 Lemen, J. R., Title, A. M., Akin, D. J., et al. 2012, *Sol. Phys.*, 275, 17  
 Leubner, M. P. 2004, *ApJ*, 604, 469  
 Lin, R. P., Dennis, B. R., Hurford, G. J., et al. 2002, *Sol. Phys.*, 210, 3  
 Livadiotis, G., & McComas, D. J. 2009, *J. Geophys. Res.*, 114, A11105  
 —. 2010, *ApJ*, 714, 971  
 —. 2013, *Space Sci. Rev.*, 175, 183  
 Mackovjak, Š., Dzifčáková, E., & Dudík, J. 2013, *Sol. Phys.*, 282, 263  
 —. 2014, *A&A*, 564, A130  
 Maksimovic, M., Pierrard, V., & Lemaire, J. F. 1997a, *A&A*, 324, 725  
 Maksimovic, M., Pierrard, V., & Riley, P. 1997b, *Geophys. Res. Lett.*, 24, 1151  
 Mason, H. E., & Monsignori Fossi, B. C. 1994, *A&A Rev.*, 6, 123  
 Meyer-Vernet, N. 2007, *Basics of the Solar Wind* (Cambridge University Press)  
 Meyer-Vernet, N., Moncuquet, M., & Hoang, S. 1995, *Icarus*, 116, 202  
 O'Dwyer, B., Del Zanna, G., Mason, H. E., Weber, M. A., & Tripathi, D. 2010, *A&A*, 521, A21  
 Owocki, S. P., & Scudder, J. D. 1983, *ApJ*, 270, 758  
 Pesnell, W. D., Thompson, B. J., & Chamberlin, P. C. 2012, *Sol. Phys.*, 275, 3  
 Petkaki, P., Del Zanna, G., Mason, H. E., & Bradshaw, S. J. 2012, *A&A*, 547, A25  
 Petkaki, P., & MacKinnon, A. L. 2011, *Advances in Space Research*, 48, 884  
 Phillips, K. J. H., Feldman, U., & Landi, E. 2008, *Ultraviolet and X-ray Spectroscopy of the Solar Atmosphere* (Cambridge University Press)  
 Poduval, B., DeForest, C. E., Schmelz, J. T., & Pathak, S. 2013, *ApJ*, 765, 144  
 Ralchenko, Y., Feldman, U., & Doschek, G. A. 2007, *ApJ*, 659, 1682  
 Schmelz, J. T., Jenkins, B. S., & Pathak, S. 2013, *ApJ*, 770, 14  
 Schmelz, J. T., Nasraoui, K., Rightmire, L. A., et al. 2009, *ApJ*, 691, 503  
 Scudder, J. D., & Karimabadi, H. 2013, *ApJ*, 770, 26  
 Stanier, A., Browning, P., & Dalla, S. 2012, *A&A*, 542, A47  
 Testa, P., De Pontieu, B., Allred, J., et al. 2014, *Science*, 346, 1255724  
 Tripathi, D., Mason, H. E., & Klimchuk, J. A. 2010, *ApJ*, 723, 713  
 Tsallis, C. 1988, *Journal of Statistical Physics*, 52, 479  
 —. 2009, *Introduction to Nonextensive Statistical Mechanics* (Springer New York, 2009)  
 Viall, N. M., & Klimchuk, J. A. 2011a, *ApJ*, 738, 24  
 —. 2011b, *ApJ*, 738, 24  
 —. 2013, *ApJ*, 771, 115  
 Vocks, C., Mann, G., & Rausche, G. 2008, *A&A*, 480, 527  
 Wang, T., Thomas, R. J., Brosius, J. W., et al. 2011, *ApJS*, 197, 32  
 Wannawichian, S., Ruffolo, D., & Kartavykh, Y. Y. 2003, *ApJS*, 146, 443  
 Warren, H. P., Ugarte-Urra, I., & Landi, E. 2014, *ApJS*, 213, 11  
 Warren, H. P., Winebarger, A. R., & Brooks, D. H. 2012, *ApJ*, 759, 141  
 Watanabe, T., Hara, H., Yamamoto, N., et al. 2009, *ApJ*, 692, 1294  
 Winebarger, A. R. 2012, in *Astronomical Society of the Pacific Conference Series*, Vol. 456, Fifth Hinode Science Meeting, ed. L. Golub, I. De Moortel, & T. Shimizu, 103  
 Young, P. R. 2010, *EIS Software Note No. 13*, ver. 4  
 Young, P. R., Watanabe, T., Hara, H., & Mariska, J. T. 2009, *A&A*, 495, 587  
 Zharkova, V. V., Arzner, K., Benz, A. O., et al. 2011, *Space Sci. Rev.*, 156  
 Zouganelis, I. 2008, *J. Geophys. Res.*, 113, A08111